

¹²L. I. Schiff, *Quantum Mechanics* (McGraw-Hill, New York, 1955).

¹³M. Abraham and R. Becker, *Theory of Electricity* (Blackie and Son, London, 1937).

¹⁴R. F. Greene, *Phys. Rev.* **141**, 687 (1966).

¹⁵*Semiconductors and Metals, Physics of III-V Compounds*, edited by R. K. Willardson and A. C. Beer (Academic, New York, 1966), Vol. 1.

¹⁶R. N. Lee (private communication).

PHYSICAL REVIEW B

VOLUME 7, NUMBER 4

15 FEBRUARY 1973

Heat-Pulse Propagation in *p*-Type Si and Ge under Uniaxial Stress*

T. Fjeldly,[†] T. Ishiguro,[‡] and C. Elbaum

Department of Physics, Brown University, Providence, Rhode Island 02912

(Received 21 June 1972)

Heat-pulse propagation has been studied in *p*-type silicon and *p*-type germanium as a function of uniaxial stress (up to 10^9 dyn cm⁻²) and of pulse temperature. The coupling between thermal phonons and the stress-split ground state of acceptors has been calculated using the effective-mass approximation for the relevant acceptor-hole wave functions. In addition to the *s*-like parts of the expansion for the envelopes usually considered, *d*-like parts of the expansion have been included here. The important phonon scattering rates due to stress-split acceptor states were derived. The rates were obtained for resonance absorption (for phonons with energies close to the splitting energy), and for several second-order processes. In addition, Rayleigh scattering of phonons by isotopic impurities has been evaluated. A black-body model for phonon emission from the heat-pulse generator was assumed. The total calculated scattering rate agrees with the observed stress dependence of the heat-pulse amplitudes when the effects of internal strains, and, in the case of high acceptor contents, of phonon multiple scattering are taken into account. A fit of the experimental results to the calculated results yields two distinct sets of values for the "static" ($a^*q \ll 1$) and "dynamic" ($a^*q \gtrsim 1$) deformation-potential constants (a^* is the effective Bohr radius of the impurity and q is the wave number of the relevant wave component). This observation resolves the apparent conflict in previously reported values of these constants, obtained from separate studies in the static (e.g., piezorefectance) and dynamic (thermal-conductivity) regimes. The present theory does not yield such distinctions for the two regimes. It is concluded, therefore, that the effective-mass approximation is not adequate for describing the full range of frequency-dependent stress effects. It should be emphasized that the heat-pulse study is particularly well suited for investigating these differences because the constants for the two regimes are derived within the framework of the same experiment.

I. INTRODUCTION

Neutral shallow impurities in semiconductors are very effective scatterers of thermal phonons at low temperatures. This has been observed as a strong increase in the thermal resistivity of Ge and Si by light doping with *n*-type¹⁻⁴ and *p*-type⁵⁻⁷ impurities. Similar effects have also been seen by propagation of heat pulses in such materials.⁸

The coupling of lattice waves to these impurities can be related to the crystal symmetry at the impurity site. For *p*-type Si and Ge, the ground state of the acceptor holes has the Γ_8 symmetry of the valence-band edge (at the center of the Brillouin zone) and is thus fourfold degenerate.⁹ These degenerate levels have been shown to contribute strongly to the thermal resistivity in *p*-type Si and Ge, because of elastic scattering of phonons.¹⁰ Any strain of lower symmetry acting on the impurity site will split the quartet into two Kramers doublets, thus giving additional scattering of phonons. The thermal conductivity is, therefore, predicted to be considerably modified by

such splitting.¹¹

We previously reported¹² the results of a preliminary study in which this coupling between acceptor holes and phonons was investigated by means of heat-pulse propagation in uniaxially stressed *p* Ge. This approach is especially well suited for systematic studies of phonon scattering by shallow impurities in semiconductors. In particular, the phonon scattering processes can be much better understood and compared more directly with theoretical predictions through heat-pulse investigations than through studies of thermal resistivity.

In this paper we present the results of heat-pulse transmission studies in uniaxially stressed boron-doped Si and gallium-doped Ge. Expressions for the relevant phonon scattering rates have been derived, from which the heat-pulse transmission was computed. The calculated and experimental results are compared and several features of the scattering processes are thereby derived.

In Sec. II a theoretical treatment is presented

for the coupling between the thermal phonons and the stress-split ground state of acceptors. This treatment is based on the effective-mass approximation for the relevant acceptor-hole wave functions. In addition, however, to the *s*-like parts of the expansion of the envelopes usually considered,^{10,11} *d*-like contributions have also been included here. By the use of a suitable hole-lattice Hamiltonian, the matrix elements for the hole transitions are calculated, from which the important phonon scattering rates are obtained. These include a resonance absorption, for phonon energies close to the splitting energy, and the rates for several second-order processes. An additional scattering mechanism of importance in the phonon-frequency range of interest here is the Rayleigh scattering from isotopic impurities. This is included in a separate consideration. The various scattering rates are combined with the black-body-radiation model for the phonon emission from the heat-pulse generator, whereby predictions for transmitted pulse energies and phonon-frequency distributions can be made.

An outline of the experimental technique and procedure is presented in Sec. III. The experimental data, consisting of heat-pulse amplitudes measured as a function of power input and of stress for several samples of Si and Ge, are presented in Sec. IV. In the same section the experimental results and the theory are compared and discussed. The comparison is carried out by computer fitting of the theoretical results to the experimental data with the use of the valence-band-edge deformation-potential constants as adjustable parameters, whereby these constants are determined. The deformation-potential constants are considered separately in the contexts of uniform static and dynamic stresses. The origin of this distinction is discussed in terms of shortcomings in the basic description of the acceptor-hole wave functions. Finally, several experimental features associated with the use of the heat-pulse technique are also discussed. These include the limitations of the black-body-radiation model, the presence of scattered phonons in the detected heat pulses, and, particularly for propagation in samples of relatively high impurity contents, resonance-broadening effects arising from local "heating" near the generator.

II. THEORY

The valence bands in Si and Ge are quite similar. The top of the band is located at the center of the Brillouin zone and has sixfold degeneracy, a threefold orbital ($L=1$) and a twofold spin degeneracy ($S=\frac{1}{2}$). This degeneracy is partially lifted by spin-orbit interaction, which splits the edge into a quadruplet and a doublet corresponding to the $J=\frac{3}{2}$

and $J=\frac{1}{2}$ states of the free atoms.

The bound states of shallow acceptor impurities can be represented by wave packets made up largely of the six Bloch waves chosen from the top of the valence band, with appropriate envelope functions to account for their localized hydrogenlike nature.⁹ The form of the wave functions of the acceptor ground-state quartet ($J=\frac{3}{2}$), specified by the magnetic quantum numbers $M_J = \frac{3}{2}, \frac{1}{2}, -\frac{1}{2},$ and $-\frac{3}{2}$ have been determined by Suzuki, Okazaki, and Hasegawa (SOH),¹³ within the framework of the effective-mass approximation. By including *s*- and *d*-like envelope parts, each wave function Ψ^{MJ} of the acceptor ground-state quartet can be represented as a linear combination of six orthogonal component vectors Φ_i^{MJ} . Of these, one ($i=0$) has purely *s*-like entries, and the remaining five ($i=1, \dots, 5$) have only *d*-like entries. Thus,

$$\Psi^{MJ} = \sum_{i=0}^5 C_i \Phi_i^{MJ}, \quad (2.1)$$

where the coefficients (amplitude factors) C_i are given by SOH. SOH also predicted explicit expressions for Φ_i^{MJ} for the axis of quantization along [001]. In the present work the corresponding expressions for the axis of quantization [111] are also needed. These have been worked out here, and are presented in Appendix A along with the values of the amplitude factors C_i and the effective Bohr radii as computed by SOH.

The coupling of phonons to the acceptor holes and the splitting of the ground-state quartet by external stressing are dealt with in terms of a strain Hamiltonian for the valence-band edge constructed from symmetry considerations by Hasegawa¹⁴:

$$H_{\text{strain}}^v = D_d^v(e_{xx} + e_{yy} + e_{zz}) + 2D_u[(L_x^2 - \frac{1}{3}L^2)e_{xx} + \text{C. P.}] + D_{u'}[(L_x L_y + L_y L_x)e_{xy} + \text{C. P.}], \quad (2.2)$$

where L_α is the α component of the angular momentum operator \vec{L} ($L=1$), $\alpha=x, y,$ or z referring to the fourfold axes. D_d^v , D_u , and $D_{u'}$ are the valence-band deformation-potential constants. C. P. denotes cyclic permutation of the indices $x, y,$ and z . $e_{\alpha\beta}$ are the conventional strain components.¹⁴

The strain Hamiltonian (2.2) can operate on the acceptor ground-state wave functions (2.1) by writing it as a 6×6 matrix on the same basis as Ψ^{MJ} . When the strain produced by uniaxial stressing is much larger than the internal strains (and the phonon strain amplitudes), it is always convenient to choose the external stress direction as the axis of quantization. Thus for [001] uniaxial stress L_α , $\alpha=1, 2, 3$ are the three components $L_x, L_y,$ and L_z of Eq. (2.2), respectively. In the case of [111] stress, $\alpha=1, 2, 3$ refer to the axes of a coordinate system with the z' axis ($\alpha=3$) along the [111] direction. The choice of the perpendicular

axes x' and y' is immaterial, but a convenient set of directions is $[1\bar{1}0]$ for x' and $[11\bar{2}]$ for y' . L_x , L_y , and L_z in Eq. (2.2) should then be decomposed along the new coordinate axes.

A. Stress-Induced Energy Splitting

When the magnitude of the valence-band-edge splitting is small compared to the ionization energy of the acceptor and the spin-orbit splitting, the effect of the external stress may be considered as a static perturbation potential acting within the ground-state quartet. In the following, the energy split for uniaxial compression along the symmetry directions $[001]$ and $[111]$ will be calculated.

By using the proper strain components for the two stress directions¹⁵ the splitting Hamiltonian becomes, according to (2.2),

$$H_{\text{strain}} = 2D_u(S_{11} - S_{12})X(L_z^2 - \frac{1}{3}L^2) \quad \text{for } \vec{X} \text{ along } [001] \quad (2.3)$$

$$= D_{u'}S_{44}X(L_z^2 - \frac{1}{2}L^2) \quad \text{for } \vec{X} \text{ along } [111], \quad (2.4)$$

where \vec{X} is the uniaxial stress and S_{11} , S_{12} , and S_{44} are the conventional compliance constants for cubic crystals. Note that Eq. (2.4) contains the angular momentum component L_z , along the $[111]$ direction. For stress along threefold or fourfold symmetry axes, the quartet splits into two doublets $M_J = \pm \frac{3}{2}$ and $M_J = \pm \frac{1}{2}$, with a separation Δ , given by

$$\Delta = \langle \Psi^{3/2} | H_{\text{strain}}^v | \Psi^{3/2} \rangle - \langle \Psi^{1/2} | H_{\text{strain}}^v | \Psi^{1/2} \rangle. \quad (2.5)$$

This results in the following expressions for the splitting:

(a) stress along $[001]$;

$$\Delta = \frac{4}{3}D_u[C_0^2 + C_1^2 - C_3^2 - \frac{1}{2}(C_2 - C_4)^2 + \sqrt{2}(C_2 + C_4)C_5] \times (S_{11} - S_{12})X; \quad (2.6)$$

(b) stress along $[111]$,

$$\Delta = \frac{2}{3}D_{u'}[C_0^2 - \frac{1}{2}(C_1 - C_3)^2 + \frac{1}{6}(3C_2^2 + 2C_2C_4 - 5C_4^2) - \frac{2}{3}\sqrt{2}(C_2 + C_4)C_5 + \frac{1}{3}C_5^2]S_{44}X, \quad (2.7)$$

where the C_i ($i=0, \dots, 5$) are the amplitude factors mentioned earlier.

For the acceptor ground states the separation Δ is often expressed in terms of the acceptor ground-state deformation-potential constants D_u^a and $D_{u'}^a$, as

$$\Delta = \frac{4}{3}D_u^a(S_{11} - S_{12})X, \quad (2.6')$$

$$\Delta = \frac{2}{3}D_{u'}^aS_{44}X. \quad (2.7')$$

Expressions (2.6) and (2.6') and (2.7) and (2.7') define D_u^a and $D_{u'}^a$ in terms of D_u and $D_{u'}$ for the case of static uniform stress.

The deformation-potential constant D_d^v of Eq. (2.2) does not enter into the stress-splitting expressions. This part of the Hamiltonian H_{strain}^v associated with D_d^v describes a shift of the center of gravity of the valence-band edge (and the acceptor states), but does not contribute to the splitting.

B. Phonon Matrix Elements

The matrix elements describing the coupling between the thermal phonons and the acceptor holes are obtained, in principle, in a straightforward manner by substituting an expansion in normal modes for the strain components into the strain Hamiltonian (2.2), and by using the acceptor ground-state wave functions discussed earlier. The axis of quantization is always chosen most conveniently along the direction of uniaxial static stress. The matrix elements will contain integrals, over all of space, of products between the various s - and d -like angular parts of the wave functions, their radial parts (see Appendix A), and a phase factor $e^{i\vec{q}\cdot\vec{r}}$ from the expansion of the strain components in normal modes. These integrals are, in general, quite involved and a complete and detailed discussion of their behavior is difficult. Essential information, however, is obtained by using form factors that reflect the admixture of d -like parts to the wave functions in an average way. One such possibility is to take the angular average over all directions of \vec{q} before evaluating the spatial integral of the matrix elements, i. e., making the substitution $e^{i\vec{q}\cdot\vec{r}} \rightarrow (\sin qr)/qr$. There are three distinct types of spatial integrals possible. The first of these involves only s -like parts; it is unaffected by the angular averaging and has the form

$$f_0 = [1 + (\frac{1}{2}qr_1)^2]^{-2}, \quad (2.8)$$

where r_1 is the effective Bohr radius for the s -like part.¹³ The second type of spatial integrals contain cross products between either s - and d -like parts or between dissimilar d -like parts; these all vanish in the present approximation because of the orthogonality properties of the spherical harmonics, and there is no contribution to the calculated coupling from the first term of H_{strain}^v [Eq. (2.2)]. The last type of integrals contain products of similar d -like parts. These are all identical and have the form

$$f_2 = \frac{1 - \frac{10}{3}(\frac{1}{2}qr_2)^2 + (\frac{1}{2}qr_2)^4}{[1 + (\frac{1}{2}qr_2)^2]^6}, \quad (2.9)$$

where r_2 is the effective radius for the d -like parts.¹³ The results obtained with the present isotropic approximation are correct in the limits $q^{-1} \ll r_2$ and $q^{-1} \gg r_2$. The error introduced for $q^{-1} \approx r_1, r_2$ may be of some significance, as will be discussed later.

TABLE I. Quasi-isotropic model for the polarization vectors.

	<i>x</i>	<i>y</i>	<i>z</i>
\hat{q}	$\sin\theta \cos\phi$	$\sin\theta \sin\phi$	$\cos\theta$
e_{q1}	$\sin\theta \cos\phi$	$\sin\theta \cos\phi$	$\cos\theta$
e_{q2}	$-\cos\theta \cos\phi$	$-\cos\theta \sin\phi$	$\sin\theta$
e_{q3}	$\sin\phi$	$-\cos\phi$	0

By adding the various contributions to the spatial integrals appearing in the matrix elements, the following two form factors (or cutoff functions) are found:

$$f^{\text{I}}(q) = C_0^2 f_0(q) + [C_1^2 - C_3^2 - \frac{1}{2}(C_2 - C_4)^2 + \sqrt{2}(C_2 + C_4)C_5] f_2(q), \quad (2.10)$$

$$f^{\text{II}}(q) = C_0^2 f_0(q) + [-\frac{1}{2}(C_1 - C_3)^2 + \frac{1}{6}(3C_2^2 + 2C_1C_4 - 5C_4^2) - \frac{2}{3}\sqrt{2}(C_2 + C_4)C_5 + \frac{1}{3}C_5^2] f_2(q). \quad (2.11)$$

In previous works based on the *s*-like approximation to the envelopes¹⁰⁻¹² there is an *a priori* frequency dependence in the acceptor ground-state deformation-potential constants used (D_u^a and $D_{u^*}^a$) because of the neglect of *d*-like and higher-order terms.^{16,17} Within the framework of the present theory, explicit expressions for the lowest-order contribution to this frequency dependence can be obtained. These are, in terms of the form factors $f(q)$, $f^{\text{I}}(q)$, and $f^{\text{II}}(q)$,¹⁸

$$D_u^a(q) = D_u [f^{\text{I}}(q)/f_0(q)], \quad (2.12)$$

$$D_{u^*}^a(q) = D_{u^*} [f^{\text{II}}(q)/f_0(q)]. \quad (2.13)$$

In the phonon matrix elements $f^{\text{I}}(q)$ is always associated with the appearance of the deformation-potential constant D_w and $f^{\text{II}}(q)$ with the appearance of D_{u^*} . For Si and Ge the numerical difference between $f^{\text{I}}(q)$ and $f^{\text{II}}(q)$ is always small; about 10% for Si in the static strain limit, and still less for $q \neq 0$. In fact, $f^{\text{I}}(q)/f^{\text{II}}(q) \rightarrow 1$ in the limit of large q . This suggests the following approximation, which is not unreasonable in relation to the other approximations made previously:

$$f^{\text{I}}(q) \approx f^{\text{II}}(q) \approx 1/2[f^{\text{I}}(q) + f^{\text{II}}(q)] = f(q). \quad (2.14)$$

With this expression, and after expanding the strain components in normal modes, the matrix elements of H_{strain}^v take on the form

$$\langle n | H_{\text{strain}}^v | n' \rangle = \sum_{qt} [\hbar\omega_{qt}/2Mv_t^2]^{1/2} (\frac{2}{3}D_{u^*}) \times (a_{qt} + a_{qt}^\dagger) C_{qt}^{nm} f(q), \quad (2.15)$$

where the acceptor ground states corresponding to $M_J = \frac{3}{2}, \frac{1}{2}, -\frac{1}{2}, -\frac{3}{2}$ are labeled by $n = 1, 2, 3, 4$, re-

spectively. ω_{qt} is an angular frequency and a_{qt} and a_{qt}^\dagger are destruction and creation operators, respectively, all for phonons of wave vector q and in the branch t . v_t is the phonon velocity in branch t and M is the crystal mass. The C_{qt}^{nm} are referred to as coupling parameters.¹⁰ Explicit expressions for these, in terms of wave-vector direction cosines and of the associated polarization vectors, have been calculated and are presented in Appendix B for the two cases of [001] and [111] stresses (i.e., axes of quantization). In order to obtain analytic expressions for the matrix elements a quasi-isotropic model for the elastic properties of the crystals has been adopted here.¹⁸ This model results in very simple expressions for the polarization vectors \vec{e}_{qt} for the three acoustical modes. These are given in Table I in terms of conventional polar angles (θ, ϕ), where $(0, \phi)$ is the [001] direction and $(\frac{1}{2}\pi, 0)$ the [100] direction. The indices 1, 2, and 3 refer to the longitudinal, fast-transverse, and slow-transverse branches, respectively. Appendix B also contains the coupling parameters C_{qt}^{nm} rewritten in terms of this model. The fictitious quasi-isotropic medium with the properties of Table I is further chosen in such a way as to represent the true elastic properties of the given crystal as closely as possible, on the average. This leads to the average velocities^{18,19}

$$\begin{aligned} \bar{v}_1 = v_L &= [(C_{11} - \frac{2}{5}C^*)/\rho]^{1/2}, \\ \bar{v}_2 = v_T &= [(C_{44} + \frac{1}{5}C^*)/\rho]^{1/2}, \end{aligned} \quad (2.16)$$

where $C^* = C_{11} - C_{12} - 2C_{44}$; C_{11} , C_{12} , and C_{44} are the three elastic constants for cubic crystals and ρ the density of the given crystal.

C. Phonon Relaxation Rates

The thermal phonons in strained *p*-type Si and Ge are scattered by various elastic and inelastic processes. For phonon energies close to the strain-induced gap, there is a strong resonance scattering due to direct hole transitions.² Another mechanism that is particularly powerful in the same region of phonon energies is the second-order elastic scattering.^{10,11,20} The present discussion is limited to the resonance scattering and all possible second-order processes, of which there are two inelastic ones, in addition to the elastic scattering just mentioned. The second-order processes all involve transitions of holes via intermediate states by elastic or inelastic scattering, or by "thermally assisted" phonon absorption,^{11,20} and therefore do not, in general, require resonance conditions.

1. Resonance Scattering

A detailed treatment of the problem of resonance scattering was carried out by Kwok²⁰ for the case

of n -type Ge. He derived the resonance attenuation of phonons, in terms of level broadening, by means of the thermodynamic Green's-function technique. The situation in n -type Ge and in strained p -type Si and Ge is quite similar, as was shown by Suzuki and Mikoshiba,¹¹ and Kwok's results can be used without difficulty here. However, the expression for the resonance scattering rate can also be derived directly by using first-order perturbation theory (Golden Rule), with all higher-order terms represented by the introduction of a level broadening Γ . Γ in turn can be calculated (also by first-order theory) as the inverse of the thermal relaxation time for the holes between the two levels. Both approaches lead to the following expression for the phonon relaxation rate due to resonance absorption¹¹:

$$\tau_R^{-1}(q, t) = \frac{\omega}{\rho v_t^2} N \frac{1 - e^{\hbar\omega/kT}}{1 + e^{-\Delta/kT}} f^2(q) \left(\frac{2}{3} D_{u^*}\right)^2 \times \sum_{m=1,4} |C_{qt}^{2m}|^2 \frac{\Gamma}{(\Delta - \hbar\omega)^2 + \Gamma^2}, \quad (2.17)$$

$$\Gamma = \Gamma_0 \coth \frac{\Delta}{2kT} = \frac{1}{4\pi} \sum_t \sum_{m=1,4} \frac{1}{\rho v_t^5} \left(\frac{\Delta}{\hbar}\right)^3 f^2\left(\frac{\Delta}{\hbar v_t}\right) \times \left(\frac{2}{3} D_{u^*}\right)^2 \langle\langle |C_{qt}^{2m}|^2 \rangle\rangle \coth\left(\frac{\Delta}{2kT}\right). \quad (2.18)$$

ω is the angular frequency of the phonon (q, t) under consideration, N is the density of impurity atoms, Δ is the level splitting due to the strain, and $\langle\langle \dots \rangle\rangle$ designates angular average.

In the quasi-isotropic model, (2.17) can be written as follows.

For \vec{X} along [001] and \vec{q} along [100],

$$\tau_R^{-1}(\vec{q}, t) = \begin{pmatrix} D^2 \\ 1 \\ 1 \end{pmatrix} \left\{ \frac{3}{4\rho v_t^2} N \left(\frac{2}{3} D_{u^*}\right)^2 \left(\frac{1 - e^{\hbar\omega/kT}}{1 + e^{-\Delta/kT}}\right) \times f^2\left(\frac{\omega}{v_t}\right) \frac{\omega\Gamma}{(\Delta - \hbar\omega)^2 + \Gamma^2}, \quad (2.19) \right.$$

where the three entries in the curly brackets are, counted from the top, associated with $t = 1, 2,$ and $3,$ respectively. $D = D_u/D_{u^*}$. Γ has the form $\Gamma = \Gamma_0 \coth(\Delta/2kT)$, where for this case

$$\Gamma_0 = \frac{1}{45\pi\rho} \left(\frac{\Delta}{\hbar}\right)^3 (D_{u^*})^2 (3 + D^2) F\left(\frac{\Delta}{\hbar}\right). \quad (2.20)$$

$F(\Delta/\hbar)$ is defined by

$$F(\Omega) = \frac{1}{v_L^5} f^2\left(\frac{\Omega}{v_L}\right) + \frac{3}{2v_T^5} f^2\left(\frac{\Omega}{v_T}\right). \quad (2.21)$$

For \vec{X} along [111] and \vec{q} along [1 $\bar{1}$ 0]

$$\tau_R^{-1}(\vec{q}, t) = \begin{pmatrix} D^2 + 2 \\ 3 \\ 3 \end{pmatrix} \left\{ \frac{N}{4\rho v_t^2} \left(\frac{2}{3} D_{u^*}\right)^2 \left(\frac{1 - e^{-\hbar\omega/kT}}{1 + e^{-\Delta/kT}}\right) \times f^2\left(\frac{\omega}{v_t}\right) \frac{\omega\Gamma}{(\Delta - \hbar\omega)^2 + \Gamma^2}, \quad (2.22) \right.$$

$$\Gamma_0 = \frac{1}{45\pi\rho} \left(\frac{\Delta}{\hbar}\right)^3 (D_{u^*})^2 2(1 + D^2) F\left(\frac{\Delta}{\hbar}\right). \quad (2.23)$$

2. Second-Order Elastic Scattering

The first term in the perturbation series for elastic scattering is of second order. In the second Born approximation, therefore, the elastic scattering rate becomes^{11,20}

$$\tau_e^{-1}(\vec{q}, t) = \frac{\pi\omega}{\rho v_t^2} \left(\frac{2}{3} D_{u^*}\right)^4 f^2(q) \sum_n N_n(T) \times \sum_{n'} \sum_{q't'} \frac{\omega_{q't'}}{2\rho v_{t'}^2} f^2(q') \delta(\omega_{q't'} - \omega) \times \left| \sum_m \left(\frac{C_{q't'}^{n'm} C_{qt}^{mn}}{E_m - E_n - \hbar\omega} + \frac{C_{qt}^{n'm} C_{q't'}^{mn}}{E_m - E_n + \hbar\omega_{q't'}} \right) \right|_{E_n = E_n^*}^2, \quad (2.24)$$

where $N_n(T)$ is the number of holes per unit volume in state n as given by the equilibrium Boltzmann distribution, i. e.,

$$N_{1,4}(T) = \frac{1}{2} N (1 + e^{\Delta/kT})^{-1}, \quad (2.25)$$

$$N_{2,3}(T) = \frac{1}{2} N (1 + e^{-\Delta/kT})^{-1}.$$

\vec{X} along [001] and \vec{q} along [100]:

$$\tau_e^{-1}(q, t) = \frac{3}{20\pi\rho^2 v_t^2} N \left(\frac{2}{3} D_{u^*}\right)^4 f^2\left(\frac{\omega}{v_t}\right) \omega^4 \times \frac{F\omega}{(\Delta^2 - \hbar^2\omega^2)^2} \left\{ \begin{array}{l} D^4\Delta^2 + 3\hbar^2\omega^2 \\ \Delta^2 + (D^2 + 2)\hbar^2\omega^2 \\ \Delta^2 + (D^2 + 2)\hbar^2\omega^2 \end{array} \right\}. \quad (2.26)$$

\vec{X} along [111] and \vec{q} along [1 $\bar{1}$ 0]:

$$\tau_e^{-1}(q, t) = \frac{N}{20\pi\rho^2 v_t^2} \left(\frac{2}{3} D_{u^*}\right)^4 f^2\left(\frac{\omega}{v_t}\right) \omega^4 \times \frac{F(\omega)}{(\Delta^2 - \hbar^2\omega^2)^2} \left\{ \begin{array}{l} (D^4 + 2)\Delta^2 + (D^4 + 6D^2 + 2)\hbar^2\omega^2 \\ 3\Delta^2 + 3(1 + 2D^2)\hbar^2\omega^2 \\ 3D^4\Delta^2 + 3D^2(D^2 + 2)\hbar^2\omega^2 \end{array} \right\}. \quad (2.27)$$

The unphysical divergencies in Eqs. (2.26) and (2.27) can be removed by once more taking into account the finite linewidths of the acceptor states. This corresponds to making the substitution¹¹ $(\Delta^2 - \hbar^2\omega^2)^{-2} \rightarrow [(\Delta^2 - \hbar^2\omega^2)^2 + 4\Gamma^2\Delta^2]^{-1}$.

3. Second-Order Inelastic Scattering

The inelastic scattering in the second order of perturbation falls into two categories. The first

is associated with hole transitions from the upper to the lower level, and the other involves hole transitions from the lower to the upper level by "thermally assisted" phonon absorption ($\omega_{\text{phonon}} < \Delta/\hbar$) or by inelastic scattering ($\omega_{\text{phonon}} > \Delta/\hbar$). The corresponding relaxation rates are, respectively,^{11,20}

$$\begin{aligned} \tau_1^{-1}(q, t) &= \frac{\pi\omega}{\rho v_t^2} \left(\frac{2}{3}D_{u'}\right)^4 (1 - e^{-\hbar\omega/kT}) f^2(q) \sum_n N_n(T) \\ &\times \sum_{n'} \sum_{q't't'} \frac{\omega_{q't't'}}{2\rho v_t^2} (n_{q't't'} + 1) f(q') \delta\left(\omega_{q't't'} - \omega - \frac{E_n - E_{n'}}{\hbar}\right) \\ &\times \left| \sum_m \left(\frac{C_{q't't'}^{n'm} C_{qt}^{mn}}{E_m - E_n - \hbar\omega} + \frac{C_{qt}^{n'm} C_{q't't'}^{mn}}{E_m - E_n + \hbar\omega_{q't't'}} \right) \right|^2, \quad (2.28) \end{aligned}$$

with $n = 1, 4$ ($M_J = \pm \frac{3}{2}$) and $n' = 2, 3$ ($M_J = \pm \frac{1}{2}$);

$$\begin{aligned} \tau_2^{-1}(q, t) &= \frac{\pi\omega}{\rho v_t^2} \left(\frac{2}{3}D_{u'}\right)^4 (1 - e^{-\hbar\omega/kT}) f^2(q) \sum_n N_n(T) \\ &\times \sum_{n'} \sum_{q't't'} \frac{\omega_{q't't'}}{2\rho v_t^2} f^2(q') \left[\epsilon n_{q't't'} \delta\left(\omega_{q't't'} + \omega - \frac{E_n - E_{n'}}{\hbar}\right) \right. \\ &\left. + (1 - \epsilon) (n_{q't't'} + 1) \delta\left(\omega_{q't't'} - \omega + \frac{E_n - E_{n'}}{\hbar}\right) \right] \\ &\times \left| \sum_m \left(\frac{C_{q't't'}^{n'm} C_{qt}^{mn}}{E_m - E_n - \hbar\omega} + \frac{C_{qt}^{n'm} C_{q't't'}^{mn}}{E_m - E_n + \hbar\omega_{q't't'}} \right) \right|^2, \quad (2.29) \end{aligned}$$

where ϵ is the step function

$$\begin{aligned} \epsilon &= 1 && \text{for } \omega < \Delta/\hbar \\ &= 0 && \text{for } \omega > \Delta/\hbar. \end{aligned}$$

It should be noted here that τ_2^{-1} does not hold when $\omega \simeq \Delta/\hbar$ (and the resonance scattering τ_R^{-1} is effective) because of the nature of the second Born approximation used. However, since τ_2^{-1} itself does not display resonance behavior, it will usually become negligible compared to τ_R^{-1} near resonance, and the error associated with retaining τ_2^{-1} over the entire frequency range is very small.

In the isotropic approximation τ_1^{-1} and τ_2^{-1} are as follows.

\vec{X} along [001] and \vec{q} along [100]:

$$\begin{aligned} \tau_1^{-1}(q, 1) &= \frac{3D^2 \left(\frac{2}{3}D_{u'}\right)^4}{20\pi\rho^2 v_1^2} N \frac{1 - e^{-\hbar\omega/kT}}{(1 - e^{-(\hbar\omega \pm \Delta)/kT})(1 + e^{\pm\Delta/kT})} \\ &\times f^2\left(\frac{\omega}{v_1}\right) \omega \left(\omega \pm \frac{\Delta}{\hbar}\right) \left(\frac{D^2 + 3}{3\hbar^2\omega^2} + \frac{D^2}{(\Delta \pm \hbar\omega)^2} \right) F\left(\omega \pm \frac{\Delta}{\hbar}\right); \quad (2.30) \end{aligned}$$

$$\begin{aligned} \tau_2^{-1}(q, \frac{2}{3}) &= \frac{3D^2 \left(\frac{2}{3}D_{u'}\right)^4}{20\pi\rho^2 v_t^2 \hbar^3} N \frac{1 - e^{-\hbar\omega/kT}}{(1 - e^{-(\hbar\omega \pm \Delta)/kT})(1 + e^{\pm\Delta/kT})} \\ &\times f^2\left(\frac{\omega}{v_t}\right) \omega (\hbar\omega \pm \Delta) F\left(\omega \pm \frac{\Delta}{\hbar}\right). \quad (2.31) \end{aligned}$$

\vec{X} along [111] and \vec{q} along [110]:

$$\tau_1^{-1}(q, 1) = \frac{\left(\frac{2}{3}D_{u'}\right)^4}{20\pi\rho^2 v_1^2 \hbar^2} N \frac{1 - e^{-\hbar\omega/kT}}{(1 - e^{-(\hbar\omega \pm \Delta)/kT})(1 + e^{\pm\Delta/kT})}$$

$$\times f^2\left(\frac{\omega}{v_1}\right) \omega \left(\omega \pm \frac{\Delta}{\hbar}\right)^3 \left(\frac{2(D^2 + 1)}{\hbar^2\omega^2} + \frac{D^2 + 2}{(\hbar\omega \pm \Delta)^2} \right) F\left(\omega \pm \frac{\Delta}{\hbar}\right); \quad (2.32)$$

$$\begin{aligned} \tau_2^{-1}(q, \frac{2}{3}) &= \left(\frac{1}{D^2} \right) \left\{ 3 \left(\frac{2}{3}D_{u'}\right)^4 / 20\pi\rho^2 v_t^2 \hbar^3 \right\} \\ &\times N \frac{1 - e^{-\hbar\omega/kT}}{(1 - e^{-(\hbar\omega \pm \Delta)/kT})(1 + e^{\pm\Delta/kT})} \\ &\times f^2\left(\frac{\omega}{v_t}\right) \omega (\hbar\omega \pm \Delta) F\left(\omega \pm \frac{\Delta}{\hbar}\right), \quad (2.33) \end{aligned}$$

where the upper and lower subscripts in $\tau_{1/2}^{-1}$ refer to the upper and lower signs on the right-hand side, respectively.

D. Other Scattering Mechanisms

In addition to the various scattering mechanisms arising from the acceptor impurities, Rayleigh scattering of phonons by isotopic impurities must be considered. This mass defect scattering has the form²¹

$$\tau_i^{-1} = A\omega^4, \quad (2.34)$$

where the constant A has the value $1.32 \times 10^{-45} \text{ sec}^3$ for Si^{7,22} and $2.40 \times 10^{-44} \text{ sec}^3$ for Ge.²²

It can be seen that this scattering is of particular importance at high frequencies ($\geq 10^{12} \text{ Hz}$). The Rayleigh scattering from the acceptor impurities themselves is quite negligible in the range of concentrations of interest here.

At the experimental temperatures (4.2 K and less) all phonon-phonon interactions are very weak, or are completely masked by the other processes, and can therefore be disregarded.

Finally then, the total scattering rate for phonons is given by

$$\tau^{-1} = \tau_R^{-1} + \tau_e^{-1} + \tau_1^{-1} + \tau_2^{-1} + \tau_i^{-1}. \quad (2.35)$$

E. Heat Pulses; Black-Body-Radiation Model

In order to be able to correlate the preceding theoretical findings with the heat-pulse measurements, it is necessary to know the frequency distribution of the heat-pulse phonons as they leave the source. It has been shown²³ that the black-body-radiation model offers a reasonable description of the situation (limitations of this model are discussed later). In this model, the energy distribution is the difference between two Planck distributions defined by the generator temperature T_p and the crystal temperature T_0 , i. e.,

$$\frac{dP}{d\nu} = \text{const} \left(\frac{\nu^3}{e^{\hbar\nu/kT_p} - 1} - \frac{\nu^3}{e^{\hbar\nu/kT_0} - 1} \right). \quad (2.36)$$

Integration of this expression over the frequency ν gives the black-body expression for the total radiated power P :

$$P = \sigma S(T_p^4 - T_0^4), \quad (2.37)$$

where S is the generator-crystal interface area and σ the Stefan constant for phonons. From Little's²⁴ work, σ can be found to be approximately 2.0×10^5 erg/sec cm² K for constantan on Si, and about 5.2×10^5 erg/sec cm² K for constantan on Ge (constantan was used for the resistive generator film in both cases). Equation (2.37) defines the generator temperature T_p to be used in expression (2.36), since P is the measured electrical power dissipated in the generator.

By introducing the various scattering mechanisms discussed previously, the resulting transmitted phonon-frequency distribution becomes

$$\frac{dP_x}{d\nu} = \frac{dP}{d\nu} e^{-x/\nu\tau}, \quad (2.38)$$

where x is the pulse path length and ν is the appropriate phonon velocity.

III. EXPERIMENTAL PROCEDURE

Five different samples of B-doped Si and two of Ga-doped Ge were used. All samples were in the shape of rectangular parallelepipeds. The impurity content, the stress and propagation directions, the dimensions, and the experimental temperatures for each sample used are listed in Table II.

The acceptor contents were evaluated by means of resistivity measurements at room temperature.²⁵ The samples were prepared with great care to ensure uniform straining during the experiment. The crystals were x-ray oriented and cut to within 1° of the orientations shown in Table II. The ends perpendicular to the stress direction were lapped and polished to be parallel within 2' of arc.

The apparatus used for applying uniaxial stress at low temperatures was designed to minimize nonuniformity of stress. The force was applied to the sample via a high-yield phosphorous-copper ring with two strain gauges (Type FNB 06-12 from BLH Electronics, Inc.) cemented on to its inner

wall for monitoring its deformation due to the force. The ring, with the strain gauges, was pre-calibrated absolutely by direct loading via a simple weight-arm system.²⁶

The heat pulses²⁷ were generated by passing short (10^{-7} sec) current pulses through a resistive constantan film (1×1 -mm area and 1000–2000 Å thick) evaporated onto one face of the specimen. A burst of thermal phonons is thereby injected into the crystal. The phonons that passed through the sample ballistically were detected on the opposite face by means of a superconducting bolometer (94-at.% In and 6-at.% Sn) kept at the onset of its superconducting-to-normal transition by a magnetic field. The bolometer had a thickness of about 5000 Å and covered an effective area of 1×1 mm (for details see Ref. 27).

In the present experiments the observed heat-pulse amplitude, measured as the peak resistance change in the superconducting bolometer, was used as a relative measure of the transmitted phonon energy. This was justified by the fact that in the nominally pure Si sample (*p*-Si 13) it was found that the detected pulse amplitude showed a clear linear dependence on the power input to the generator, over a range of several decades. At higher input powers (typically above 1 W) a non-linear dependence was observed and attributed to a shift of the emitted phonon frequency envelope towards higher frequencies, with a resulting increase in phonon scattering in the "pure" sample (due to isotopes, phonon-phonon interactions, etc.). Furthermore, no stress dependence in the heat-pulse amplitude was found. Therefore, from measurements on the nominally pure control sample *p*-Si 13, the following three conclusions could be drawn: (a) The characteristics of the detector and generator films do not change measurably with the application of external uniaxial stress to the sample (at least up to 10^9 dyn/cm²). (b) Any dependence of the transmitted heat-pulse amplitude on stress for the other samples can be attributed to the acceptor impurities (assuming everything else equal). (c) The detectors can be assumed to have

TABLE II. Acceptor content, orientation, dimensions, and experimental temperature for the various samples.^a

Sample	Impurity content (cm ⁻³)	Stress direction	Propagation direction	Dimensions ^b	Experimental temperature
<i>p</i> -Si 13	$< 1 \times 10^{14}$ B	[001]	[100]	$10 \times 4 \times 3$	3.36–4.01
<i>p</i> -Si 15A	1×10^{15} B	[001]	[100]	$15.4 \times 3.2 \times 2.1$	3.36
<i>p</i> -Si 15B	1×10^{15} B	[111]	[$\bar{1}\bar{1}0$]	$16.2 \times 3.8 \times 2.75$	3.36
<i>p</i> -Si 16A	8×10^{15} B	[001]	[100]	$14.6 \times 4.0 \times 2.6$	3.36
<i>p</i> -Si 16B	8×10^{15} B	[111]	[$\bar{1}\bar{1}0$]	$16.1 \times 3.75 \times 2.7$	3.80
<i>p</i> -Ge 14	5×10^{14} Ga	[111]	[$\bar{1}\bar{1}0$]	$9.0 \times 4.0 \times 2.9$	3.36
<i>p</i> -Ge 16	1.7×10^{16} Ga	[111]	[$\bar{1}\bar{1}0$]	$9.0 \times 4.2 \times 2.8$	4.23

^a*p*-Si 13 supplied by Texas Instruments, *p*-Si 15 and *p*-Si 16 by Semimetals, Inc., *p*-Ge 14 and *p*-Ge 16 by R. C. A.

^bThe dimensions in the stress directions are given first, and in the propagation direction second.

a linear response (when measuring transmitted pulse amplitudes) to the phonon energy in the observed pulse.

IV. RESULTS AND DISCUSSION

A. Experimental Results

Typical observed heat pulses in the samples *p*-Si 15A and *p*-Si 16B as a function of applied stress are shown in Figs. 1 and 2. Examples of data on the heat-pulse amplitude vs stress, for various input power levels, are presented in Figs. 3–10. The typical experimental uncertainty in the data is 10%, both in stress and in amplitude, but may be as much as 30% in the amplitude at the smallest signal levels shown in Figs. 7–9.

Both longitudinal and transverse waves were investigated for propagation along the [100] and the [110] directions (with stress parallel to [001] and [111], respectively). For wave propagation along [100], the transverse branches are degenerate, but along [110] there should be two separate transverse pulses. However, because of phonon focusing,^{28–30} materials with the elastic properties of Si and Ge have a strongly enhanced fast-transverse wave and a reduced slow-transverse wave in the [110] direction. Because of the small temporal separation between the two pulses as they arrive at the detector, and the large difference in amplitude, the slow-transverse wave becomes difficult to measure reliably in the presence of the fast-transverse wave. Therefore, only the fast-transverse and the longitudinal pulses have been measured in this direction.

B. Theoretical Fits for *p*-Si 15, *p*-Ge 14, and *p*-Ge 16

The curves drawn through the experimental points in Figs. 3–10 are computer-fitted theoretical results based on the scattering rates given in

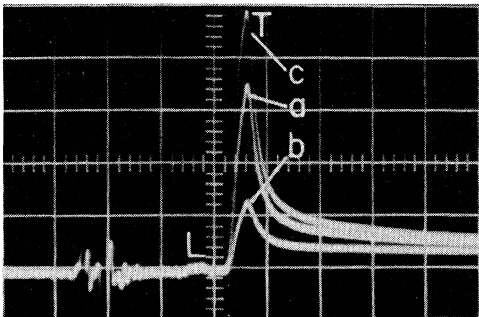


FIG. 1. Heat pulses in sample *p*-Si 15A. Input power, 0.3 W (i. e., $T_{\text{pulse}} = 6.5$ K as determined from the black-body theory). Vertical and horizontal scales are 0.05 V/div. and 0.2 $\mu\text{sec}/\text{div.}$, respectively. The propagation is along the [100] direction, a distance of 3.2 mm. *a*, *b*, and *c* are pulses for external stresses 0, 5.3, and 11.4 ($\times 10^8$ dyn/cm²), respectively, along the [001] direction.

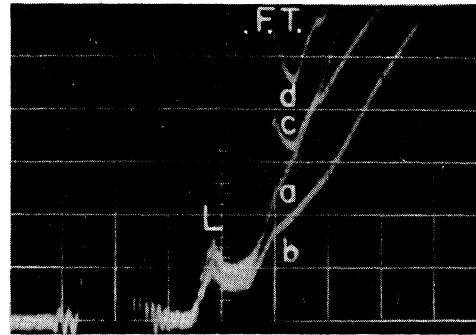


FIG. 2. Heat pulses in sample *p*-Si 16B. Input power, 3.9 W (i. e., $T_{\text{pulse}} = 12.1$ K as determined from the black-body theory). Vertical and horizontal scales are 0.02 V/div. and 0.2 $\mu\text{sec}/\text{div.}$, respectively. The propagation is along the [110] direction, over a distance of 3.8 mm. *a*, *b*, *c*, and *d* are pulses for external stresses 0, 2.0, 4.2, and 4.7 ($\times 10^8$ dyn/cm²), respectively, along the [111] direction. F. T. denotes the fast-transverse pulse and L the longitudinal pulse.

Sec. II and on the black-body-radiation model for the phonon emission from the generator [Eq. (2.37)]. The conversion from the applied uniaxial stress to the physically important acceptor ground-state splitting Δ is performed by using the expressions (2.6) and (2.7). These conversion formulas, and the scattering rates due to the acceptor impurities, both contain the valence-band deformation-potential constants D_u and D_u' . These constants are determined by the fitting procedure. The appearance of D_u and D_u' in the two contexts arises from different physical circumstances. In the case of the scattering rates they are associated with the rapidly oscillating strains due to the phonons, and in the conversion formulas they are related to external static stress. A rigorous treatment of the problem should yield a single frequency-independent value for the deformation-potential constant. The best fits were obtained, however, by using different values for these constants in the contexts of static and of dynamic stresses. It is useful, therefore, to consider the two sets of values as independent operational parameters whose differences can be interpreted as reflecting the shortcomings in the theory used. In particular, the description of the acceptor envelopes (used here) is expected to be insufficient, especially for Ge which has considerable anisotropy in the envelope functions. In the case of Si the acceptor levels are deeper than in Ge, and the effective-mass theory is not expected to give a sufficiently precise description for the interactions under consideration. The differences in the corresponding "static" and "dynamic" constants found here may provide a measure of these discrepancies.

Except for the two samples *p*-Si 16A and *p*-Si 16B, use of the black-body-radiation model gave rea-

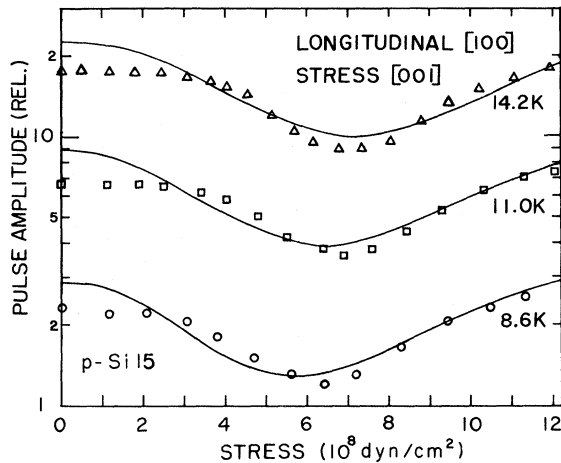


FIG. 3. Amplitude vs stress for longitudinal heat pulses in the [100] direction in sample *p*-Si 15A, with stress along [001]. The solid curves are theoretical fits to the experimental data. The numbers on the right represent black-body pulse temperatures for the various curves. According to the fits, a stress of 1×10^8 dyn/cm² is found here to represent an acceptor ground-state splitting of about 4.3 K.

sonable fits between theory and experiment for all cases of higher pulse temperatures. This corresponds with observations made by others,²³ showing that the black-body model applies well if the pulse (generator) temperature (as determined by this model) is sufficiently high, typically above 10 K. At these temperatures the mean free path of the phonons in constantan is roughly of the order of the film thickness,²⁹ i.e., an approximate thermal equilibrium can be established. At lower generator temperatures the mean free path is longer and a substantial portion of the initially produced phonons can escape without participating in the thermalization. Besides, in the metal film, with decreasing temperature the fraction of thermal energy associated with the electrons increases, which makes the description of the phonon generation quite difficult at the lower input powers. At the smaller pulse temperatures, at which isotope scattering is relatively ineffective, the present theory predicts a shift in the minimum of the pulse amplitude-vs-stress curves towards lower stresses. The corresponding experimental curves showed similar shifts, but by lesser amounts. This would indicate that the actual phonon frequency envelope was more pronounced at the higher frequencies than predicted by this black-body model. An *indication* of the experimental phonon frequency distribution at the low input powers might be obtained in terms of an effective pulse temperature parameter. This was done by using the (black-body) pulse temperature as a new fitting param-

eter, while employing the deformation-potential constants obtained at the higher pulse powers, where the black-body model is expected to apply. These fits are shown as dashed curves in the figures.

The relative heights of the theoretical curves representing different input power levels (pulse temperatures) have been adjusted to agree with the respective experimental data sets. It was generally observed for the doped samples that the pulse amplitude, for a given stress, grew faster with increasing power input to the source than predicted by the present theory. This should be expected since the theory does not include secondary effects such as the admixture of scattered phonons to the ballistic pulse as it arrives at the detector, the related problem of backscatter to the source within the width of the driving pulse, and the shift from the assumed thermal equilibrium of the local distribution within the duration of the heat pulse. A further possible source of discrepancy is the uncertainty in the determination of the Stefan constant σ of Eq. (2.37).

C. Results for *p*-Si 16

The experimental data for the highest acceptor concentration samples used, *p*-Si 16A and *p*-Si

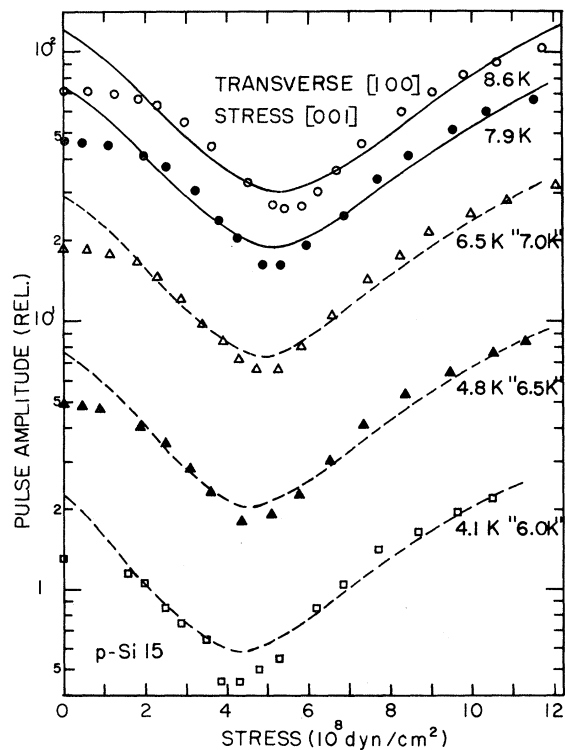


FIG. 4. Same as Fig. 3 but for propagation of transverse waves. The numbers in quotation marks represent effective temperatures (see text) referring to the dashed fits. 1×10^8 dyn/cm² here corresponds to a level splitting of 4.8 K.

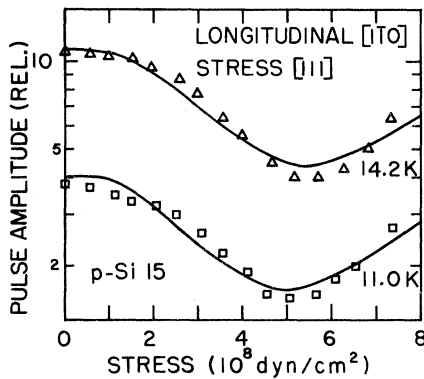


FIG. 5. Amplitude vs stress for longitudinal heat pulses in the [110] direction in sample *p*-Si 15B, with stress along [111]. The solid curves represent theoretical fits to the experimental data. The numbers on the right are the black-body temperatures for the various curves. According to these fits, a stress of 1×10^8 dyn/cm² corresponds to an acceptor ground-state splitting of about 5.6 K.

16B, could not be fitted directly with the present theory, except for a coincidence in the trends at the highest applied stresses. The experimental

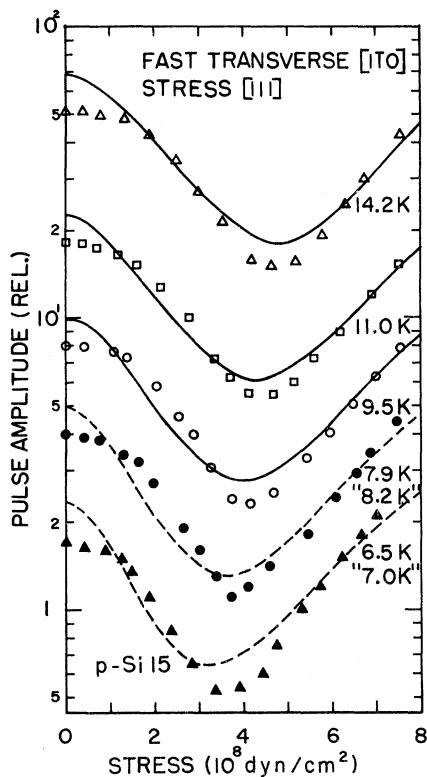


FIG. 6. Same as Fig. 5, but for fast-transverse waves. The numbers in quotation marks represent effective temperatures, referring to the dashed fits. 1×10^8 dyn/cm² corresponds to a level splitting of about 6.1 K.

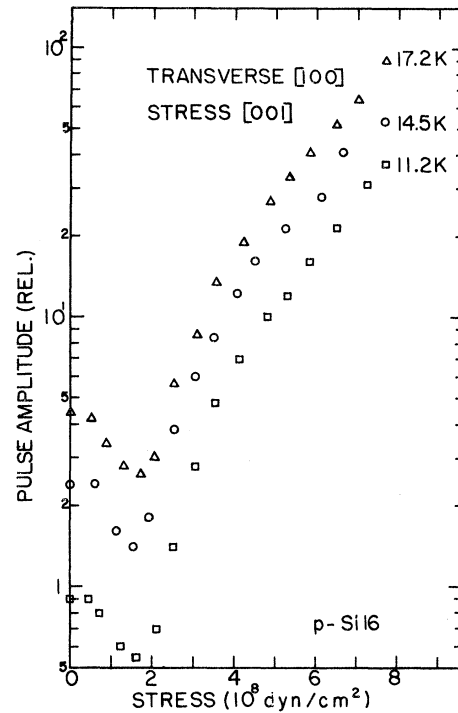


FIG. 7. Amplitude vs stress for transverse heat pulses in the [100] direction in sample *p*-Si 16A. The numbers on the right represent the black-body temperatures for the various experimental data sets.

data indicate that the phonon scattering is much stronger than predicted at the lower stress levels. Figure 2 shows that especially for small stresses the scattering is so strong that clear ballistic pulses are not seen. There are, however, points of qualitative agreement between the theory and the experiment, such as (a) the presence of a minimum in the stress-vs-amplitude curves, which indicates the presence of a resonance scattering, and (b) a strong increase in the pulse amplitude at high stress (see Figs. 7-9).

The discrepancies at lower stresses are the following: (a) The experimental amplitude is consistently lower than the theoretical, by up to a factor of 5 in the case of the longitudinal pulse, and by as much as a factor of 100 for transverse pulses propagating along [100] with stress along [001]. (b) Particularly for transverse waves, the minima in the experimental curves are located at lower stresses than in the corresponding theoretical curves, with the former at 30-50% of the latter. The minima of the theoretical curves are generally wide, while the experimental curves are rather narrow with a sharp increase on the high-stress side. (c) Most of the experimental stress-vs-amplitude curves exhibit a characteristic "knee" at the high-stress side of the minimum, where the very rapid increase in the amplitude is

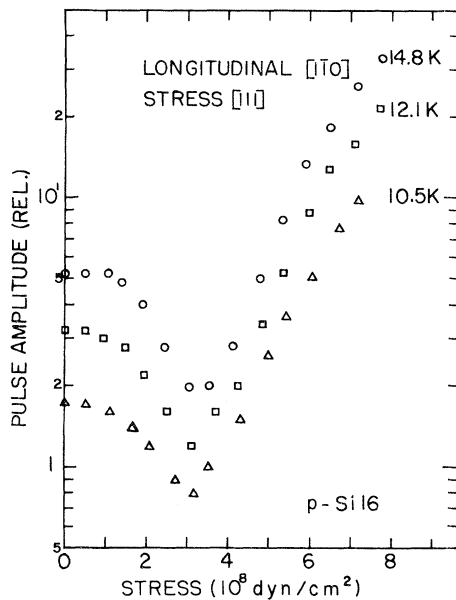


FIG. 8. Amplitude vs stress for longitudinal heat pulses in the $[1\bar{1}0]$ direction in sample p -Si 16B. The numbers on the right represent the black-body temperatures for the various data sets.

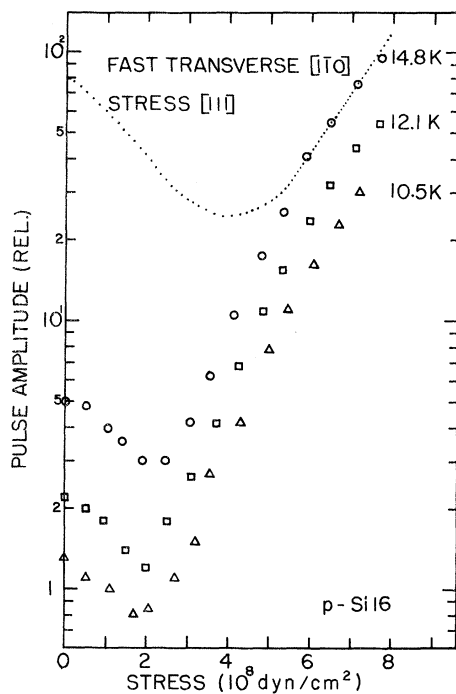


FIG. 9. Same as Fig. 8, but for fast-transverse waves. The dotted curve is the theoretical fit to the upper data set when local heating and the resulting level broadening is neglected. The curve was obtained by using the fitting parameters found for fast-transverse waves in p -Si 15B.

followed by an increase that is in closer agreement with the theory. The features listed above are all consistent with the presence of additional scattering. Several sources of such scattering have been examined, and it was found that among these sources secondary effects associated with the strong primary scattering due to the high impurity content are the most likely explanation. Such a secondary effect can be interpreted as a broadening of the resonance interaction and is attributed to the increase in phonon density near the generator, where the phonon scattering is particularly high. An estimate based on the assumption that the total energy dissipated in the generator within one pulse is used to heat up a substrate volume of $(1 \times 1 \text{ mm}) \times \lambda$ ($1 \times 1 \text{ mm}$ is the generator area, $\lambda \approx 1 \text{ mm}$ is the calculated characteristic decay distance for the pulse), yields a temperature in that region of about 10 K for p -Si 16. Assuming a helium-bath temperature of 3.5 K, we find that the relative increase in the resonance broadening due to this heating becomes $\Gamma_{10}/\Gamma_{3.5} = \coth(\Delta/20)/\coth(\Delta/7)$ [according to Eq. (2.18)], where Δ is the ground-state splitting in Kelvin. $\Gamma_{10}/\Gamma_{3.5}$ is about 2.9 for $\Delta = 0 \text{ K}$, 1.9 for $\Delta = 10 \text{ K}$, 1.3 for $\Delta = 20 \text{ K}$, and tends to 1 for increasing Δ .

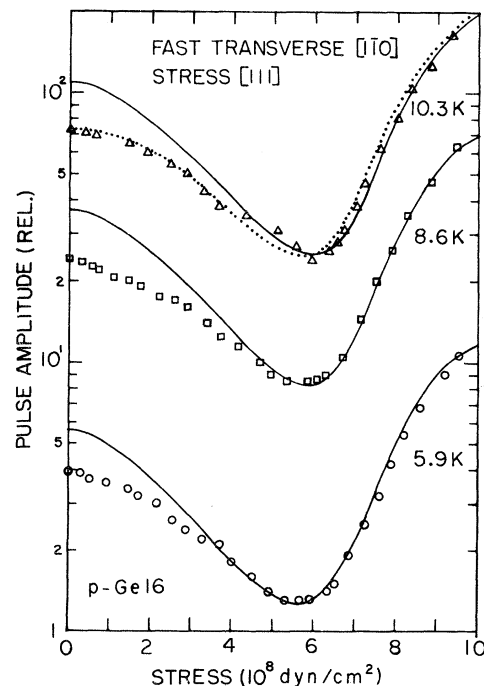


FIG. 10. Amplitude vs stress for fast-transverse heat pulses in the $[1\bar{1}0]$ direction in the sample p -Ge 16, with stress along $[111]$. The dotted curve fitted to the upper experimental series is corrected for internal strains. $1 \times 10^8 \text{ dyn/cm}^2$ is found here to correspond to a splitting energy of about 2.8 K.

This broadening will make the scattering more effective over a wider frequency range, but the peak scattering rate will be reduced. The total net effect, including the cumulative effect of the induced scattering due to the broadening, is difficult to calculate, but preliminary estimates show an enhancement of the scattering at low stresses in agreement with the experimental observation. Furthermore, the effect vanishes for higher stresses ($\Gamma_{10}/\Gamma_{3,5} \rightarrow 1$), and is consistent with the agreement obtained between theory and experiment in that region.

The strong additional scattering observed for the *p*-Si 16 samples was not present for the even more highly doped Ge sample *p*-Ge 16. This is consistent with the fact that the coupling of phonons to acceptor impurities is weaker in Ge than in Si. This manifests itself as a generally lesser thermal broadening of the resonance in Ge.

D. Effects of Internal Strains

In performing the fitting of the theory to the experimental heat-pulse data for *p*-Si 15A and *p*-Si 15B, *p*-Ge 14 and *p*-Ge 16, consideration should be given to the presence of internal static strains due to crystal defects (e.g., the acceptor impurities themselves, dislocations, vacancies, etc.), and to dynamic strains such as the Jahn-Teller effects. These strains cause a splitting of the acceptor ground state, and act in addition to the externally applied stress. Corrections for the internal strains can be carried out (to lowest order) by approximating the (unknown) distribution of internal stresses acting on the impurities by a force per unit area of *average* magnitude *p* and random direction. This is then added vectorially to the externally applied force (per unit area) *x*. By averaging over many impurities, we find that the total stress *X* is given by

$$\begin{aligned} X &= x + p^2/3x, & x > p \\ &= p + x^2/3p, & x \leq p. \end{aligned} \quad (4.1)$$

p has been chosen to correspond to the theoretical (uncorrected) pulse amplitude, when this is equal to the amplitude measured at zero external stress. With this correction, the theoretical and experimental amplitude-vs-stress curves are made to coincide at zero external stress. The stress correction to the theoretical curve by Eq. (4.1) is about 30% at $x = p$, and drops rapidly to less than 10% at $x = 2p$. Thus for internal stresses corresponding to the low to intermediate stress region, there will be almost no correction to the results obtained from the higher external stresses. The consequences of this correction for deformation-potential parameters determined by the fitting of

the theory to the experimental data, are very small, usually less than the uncertainty in the fitting itself. In order to preserve clarity, the internal stress corrections are not shown in Figs. 3-10, except as an example in Fig. 10 (shown as a dotted curve through the upper data set). However, *p* has been determined from the various data sets for *p*-Si 15A, *p*-Si 15B, and *p*-Ge 16. It should be noted that the internal strains serve to explain why the pulse amplitude for *p*-Si 16A and *p*-Si 16B is depressed at zero external stress. At $\Delta = 0$ it should be expected that all broadening effects would disappear, since $\Gamma(\Delta = 0) = 0$, but with the presence of internal strain this condition is really never achieved.

E. Deformation-Potential Constants

By taking into consideration the matters discussed so far, the fitting of the theory to the experimental data for the samples *p*-Si 15A and *p*-Si 15B, *p*-Ge 14 and *p*-Ge 16 resulted in the deformation-potential parameters shown in Table III. In the same table is also shown the average internal stress *p*, as determined for Figs. 3-6, 9, and 10.

A comparison of the deformation-potential constants found for the various experimental circumstances indicates that there is reasonable internal consistency between the results obtained both for Si and Ge. In Si, however, the static constants are, in general, higher in value than the dynamic constants by about 30% for D_u and by 25% for $D_{u'}$. In Ge the situation is reversed, with $D_{u'}$ (dynamic) larger than D_u (static) by about 25% for *p*-Ge 16 and 45% in the case of *p*-Ge 14. The spread of values obtained for the static and the dynamic constants, considered separately, was small and usually within the fitting uncertainty.

The deformation-potential constants D_u and $D_{u'}$ have been measured by others, with considerable disagreement between the various values quoted. Thus for Ge the following values for ($D_u, D_{u'}$) (in eV) have been reported: (3.2, 6.1),³¹ (4.1, 4.1),³² (3.6, 3.6),³³ (3.9, 4.1),³⁴ and (3.8, 3.1).³⁵ These were all obtained by optical methods (piezospectroscopy and piezoreflectance), and belong in the category of *static* stress. For Si the following values have been reported: (2.0, 2.7),¹⁵ (3.2, 4.2),³⁶ (3.6, 4.6),³⁷ (3.2, 2.7).³⁸ The results in Table III compare reasonably well with the various constants quoted here, if the disagreement between the values obtained by the different authors is considered.

It should be emphasized that the present experiments give the valence-band deformation-potential constants D_u and $D_{u'}$ only indirectly. The actual physical system under consideration is the collection of holes bound to acceptor impurities, instead of free holes at the valence-band edge, for

TABLE III. Deformation-potential constants for the valence-band edge of Si and Ge obtained from theoretical fitting to experimental heat-pulse data. Also shown are average internal stresses determined from the fitting.

Sample	Phonon branch	Static		Dynamic		Average internal stress, p (10^8 dyn/cm 2)
		D_u	D'_u	D_u	D'_u	
<i>p</i> -Si 15A	Long.	3.7 ± 0.4		3.1 ± 1.0	5.3 ± 0.5	2.6 ± 1.0
	Trans.	3.9 ± 0.4		2.5 ± 1.0	4.7 ± 0.5	1.6 ± 0.8
<i>p</i> -Si 15B	Long.		6.8 ± 0.7	2.5 ± 1.0	5.0 ± 0.5	1.2 ± 0.7
	Fast trans.		6.2 ± 0.7	2.5 ± 1.0	4.7 ± 0.5	1.0 ± 0.6
<i>p</i> -Ge 14	Fast trans.		3.7 ± 0.4	6.2 ± 2.0	6.9 ± 1.0	1.6 ± 0.8
<i>p</i> -Ge 16	Fast trans.		4.0 ± 0.4	4.7 ± 2.0	5.3 ± 0.5	2.1 ± 0.6

which D_u and $D_{u'}$ are directly applicable. In particular, the possible influence of the chemical effects of the impurities on the results have not been taken into account in the present discussion. The values of D_u and $D_{u'}$ obtained here should therefore, strictly speaking, be considered as characteristic for the localized acceptor holes rather than for free holes at the valence-band edge. It may also be noted that $D_u^a(0)$ and $D_{u'}^a(0)$ are calculable from Eqs. (2.12) and (2.13) with the use of the static values of D_u and $D_{u'}$.

F. Calculations of Transmitted Phonon Spectra

In conjunction with the fitting procedure, the various relaxation rates (Sec. II) were computed. These results show that the resonant term τ_R^{-1} and the resonant fluorescence term τ_e^{-1} give the strongest contribution to the scattering in the low to intermediate frequency range, when moderate stresses are applied. In the high-frequency region, typically above 4×10^{11} Hz in Ge and 8×10^{11} Hz in Si (for the doping levels shown), the isotope scattering τ_i^{-1} is the most powerful and tends to mask the effects of the acceptor impurities. The maximum in the black-body energy distribution is at about 6×10^{11} Hz for a pulse temperature of 10 K, and an ambient temperature in the liquid-helium range. The transmitted heat pulses are therefore, in general, strongly affected by the isotope scattering edge, particularly in Ge where the typical pulse frequency distribution is truncated by this scattering below the black-body maximum. This is the reason why the minimum in the amplitude-vs-stress curves (Fig. 10) does not shift measurably with the pulse temperature in Ge. In Si, because of the higher cutoff frequency, the maximum in this distribution can be moved appreciably by changing the pulse temperature. This is reflected in the amplitude-vs-stress curves for Si (Figs. 3-9). The phonon frequency distributions for the transmitted pulses have been calculated on the basis of the relaxation rates discussed above, with the assumption of a black-body emission of phonons from the generator. Some of

these results are presented in Figs. 11-14. The curves illustrate clearly the effects of the important scattering mechanisms. The resonance scattering is seen to create a strong dip in the distribution that shifts towards higher frequencies with increasing stress splitting. The isotope scattering results in a fairly sharp cutoff in the distribution at the high-frequency end. The areas under the distribution curves represent the total transmitted heat-pulse energy. These were the results fitted to the experimental data. The ratio of the transmitted to the total injected pulse energies has been computed for the various experimental conditions and is presented in Table IV.

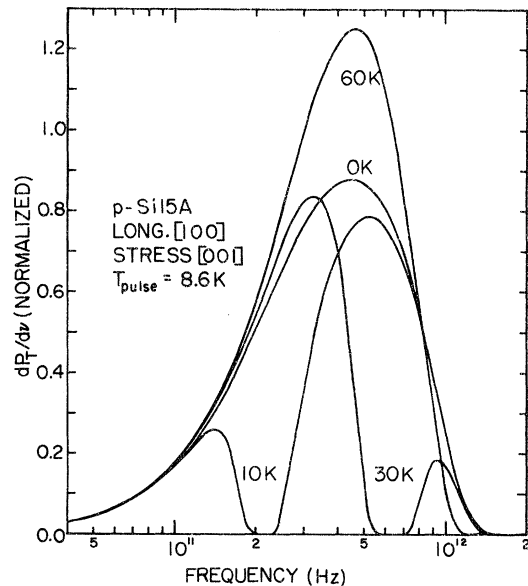


FIG. 11. Phonon frequency distributions for transmitted longitudinal heat pulses in sample *p*-Si 15A, calculated for different values of the acceptor ground-state splitting (shown in K), and on the basis of black-body radiation from the generator. The ordinate is normalized to give an area of kT_p/h under the distribution curves when no scattering is present. In these calculations a crystal temperature of 3.36 K was assumed.

TABLE IV. Computed unscattered fractions of the heat pulses.

$\Delta(K)$ $T_p(K)^a$	0		10		20		30		40		50		60	
	L^b	T	L	T										
14.2	0.325		0.284		0.187		0.145		0.170		0.242		0.327	
11.0	0.438		0.37		0.231		0.199		0.260		0.370		0.477	
<i>p</i> -Si 15A 8.6	0.538	0.346	0.430	0.193	0.259	0.101	0.264	0.179	0.374	0.105	0.515	0.308	0.628	0.451
7.9	0.366		0.193		0.103		0.118		0.206		0.206		0.347	
6.5, "7.0"	0.391		0.188		0.106		0.141		0.250		0.250		0.406	
4.8, "6.5"	0.405		0.183		0.109		0.157		0.278		0.278		0.442	
4.1, "6.0"	0.419		0.177		0.113		0.177		0.310		0.310		0.480	
14.2	0.276	0.143	0.238	0.092	0.147	0.050	0.111	0.037	0.138	0.056	0.208	0.108	0.292	0.185
<i>p</i> -Si 15B 11.0	0.375	0.192	0.313	0.114	0.184	0.061	0.159	0.057	0.219	0.096	0.326	0.178	0.434	0.279
9.5	0.220		0.122		0.066		0.072		0.128		0.128		0.358	
7.9	0.252		0.124		0.073		0.097		0.178		0.178		0.308	
6.5, "7.0"	0.271		0.121		0.079		0.119		0.218		0.218		0.363	
17.2	0.025	0.007	0.017	0.005	0.012	0.002	0.011	0.002	0.020	0.003	0.042	0.006	0.080	0.015
<i>p</i> -Si 16A 14.5	0.031	0.008	0.019	0.005	0.014	0.003	0.016	0.002	0.031	0.004	0.062	0.009	0.115	0.023
11.2	0.039	0.009	0.021	0.006	0.019	0.004	0.028	0.004	0.056	0.007	0.109	0.018	0.191	0.042
14.8	0.026	0.007	0.015	0.004	0.011	0.002	0.014	0.002	0.027	0.004	0.054	0.010	0.098	0.023
<i>p</i> -Si 16B 12.1	0.032	0.007	0.017	0.004	0.014	0.003	0.022	0.003	0.044	0.007	0.084	0.016	0.148	0.036
10.5	0.035	0.007	0.017	0.004	0.017	0.003	0.030	0.005	0.060	0.010	0.113	0.022	0.192	0.049
$\Delta(K)$	0		5		10		15		20		25		30	
$T_p(K)$	L	T												
<i>p</i> -Ge 14 6.6	0.064	0.219	0.049	0.174	0.029	0.118	0.019	0.115	0.029	0.202	0.072	0.256	0.118	0.267
10.3	0.064	0.047	0.049	0.036	0.029	0.020	0.019	0.014	0.029	0.017	0.072	0.061	0.118	0.094
<i>p</i> -Ge 16 8.6	0.064	0.064	0.048	0.048	0.026	0.026	0.015	0.015	0.024	0.024	0.087	0.087	0.132	0.132
5.9	0.102	0.102	0.075	0.075	0.039	0.039	0.024	0.024	0.046	0.046	0.161	0.161	0.239	0.239

^aThis column shows both theoretical (i. e., black-body) and effective pulse temperatures, the latter in quotation marks. When effective temperatures are listed, these have been used in the computations.

^b L means the longitudinal branch, and T the relevant transverse branch (i. e., degenerate transverse for the propagation along [100], and fast transverse for propagation along [110]).

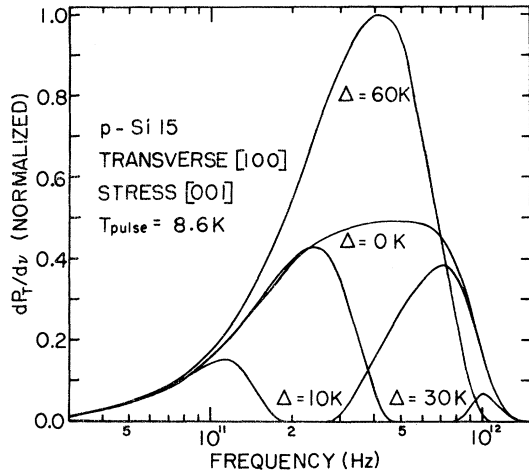


FIG. 12. Same as Fig. 11, but for propagation of transverse waves.

The computations were performed using the relevant deformation-potential constants and effective temperatures obtained in the fitting procedure. The numerical constants used in the calculations are listed in Table V.

V. SUMMARY

Interaction of thermal phonons with stress-split acceptor impurity states in semiconductors at liquid-helium temperatures has been demonstrated by means of heat-pulse experiments. The depen-

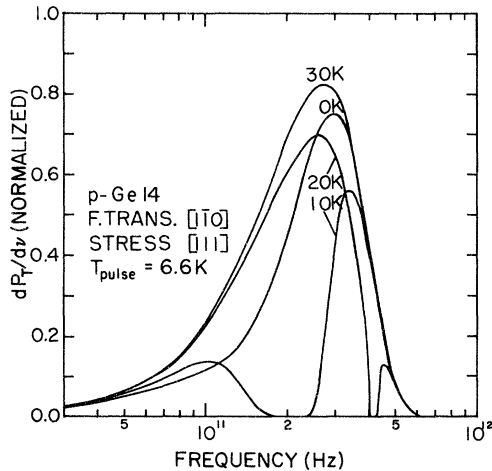


FIG. 13. Phonon frequency distributions for transmitted fast-transverse heat pulses in the sample *p*-Ge 14, calculated for different values of the acceptor ground-state splitting (shown in K), and on the basis of black-body radiation from the generator. The ordinate is normalized to give an area of kT_p/h under the distribution curves when no scattering is present. In these calculations a crystal temperature of 3.36 K was assumed.

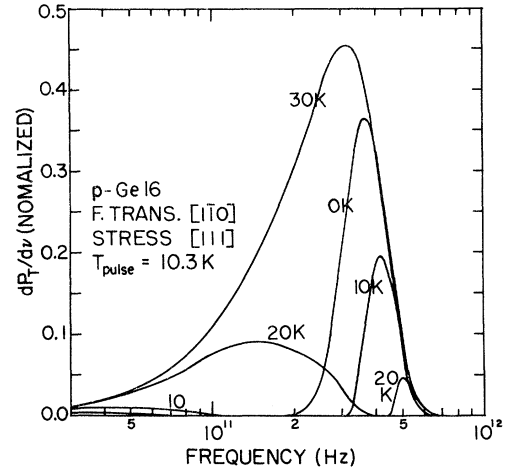


FIG. 14. Phonon frequency distributions for transmitted fast-transverse heat pulses in the sample *p*-Ge 16, calculated for different values of the acceptor ground-state splitting (shown in K), and on the basis of black-body radiation from the generator. The ordinate is normalized to give an area of kT_p/h under the distribution curves when no scattering is present. In these calculations a crystal temperature of 4.23 K was assumed.

dence of this interaction on external uniaxial stress was studied both theoretically and experimentally. In particular, the coupling between thermal phonons and acceptor holes in the stress-split acceptor ground state in Si and Ge was investigated.

The theoretical treatment is based on the effective-mass approximation for the description of the acceptor states. *d*-like contributions to the relevant wave functions have been included, as

TABLE V. Numerical constants used. ρ , v_1 , v_2 , S_{11} , S_{12} , and S_{44} are given in Ref. 39. For v_L and v_T see Ref. 10. r_1 , r_2 , and c_i , $i=0, \dots, 5$ are presented in Ref. 13. σ was computed from Ref. 24. A is given in Refs. 7 and 22.

Symbol	Si	Ge	Dimension
ρ	2.33	5.32	g/cm^3
$v_1[100]$	8.48×10^5	4.92×10^5	cm/sec
$v_1[1\bar{1}0]$	9.18×10^5	5.41×10^5	cm/sec
$v_2[100] (=v_3)$	5.87×10^5	3.55×10^5	cm/sec
$v_2[1\bar{1}0]$	5.87×10^5	3.55×10^5	cm/sec
v_L	9.33×10^5	5.37×10^5	cm/sec
v_T	5.42×10^5	3.28×10^5	cm/sec
$S_{11} - S_{12}$	0.98×10^{-12}	1.20×10^{-12}	cm^2/dyn
S_{44}	1.26×10^{-12}	1.47×10^{-12}	cm^2/dyn
r_1	1.50×10^{-7}	3.78×10^{-7}	cm
r_2	1.11×10^{-7}	2.99×10^{-7}	cm
c_0	0.932	0.860	
c_1	-0.014	-0.198	
c_2	-0.351	-0.318	
c_3	0.022	0.187	
c_4	0.080	0.292	
c_5	0.004	0.002	
σ	2.00×10^5	5.20×10^5	$\text{erg/sec cm}^2 \text{K}^4$
A	1.32×10^{-45}	2.40×10^{-44}	sec^3

TABLE VI. The functions $\Phi_i^{M_J}$ for axis of quantization along [001] [$a=z^2-\frac{1}{2}(x^2+y^2)$, $b=x^2-y^2$, $c=z(x-iy)$, $d=ixy$], with corresponding radial functions and amplitude factors.

M_J					Radial parts	Amplitudes c_i	
	$\frac{3}{2}$	$\frac{1}{2}$	$-\frac{1}{2}$	$-\frac{3}{2}$		Si	Ge
$\Phi_0^{M_J}$	1	0	0	0	$\frac{1}{(4\pi)^{1/2}} R_0(r)$	0.932	0.860
	0	1	0	0			
	0	0	0	0			
	0	0	0	0			
	0	0	1	0			
$\Phi_1^{M_J}$	0	0	1	0	$\left(\frac{5}{4\pi}\right)^{1/2} \frac{R_1(r)}{r^2}$	-0.014	-0.198
	$\frac{1}{2}a$	0	$\sqrt{3}b/4$	0			
	0	$-\sqrt{2/3}a$	0	0			
	$\frac{3}{4}b$	0	$a/2\sqrt{3}$	0			
	0	$a/2\sqrt{3}$	0	$\frac{3}{4}b$			
$\Phi_2^{M_J}$	0	0	$-\sqrt{2/3}a$	0	$\left(\frac{5}{4\pi}\right)^{1/2} \frac{R_2(r)}{r^2}$	-0.351	-0.318
	0	$\sqrt{3}b/4$	0	$\frac{1}{2}a$			
	0	$c^*/\sqrt{2}$	$-d/\sqrt{2}$	0			
	$\sqrt{3}c/2$	0	$-c^*/2$	0			
	$\sqrt{3/2}d$	$-c/\sqrt{2}$	0	0			
$\Phi_3^{M_J}$	0	0	$c^*/\sqrt{2}$	$-\sqrt{3/2}d$	$\left(\frac{5}{4\pi}\right)^{1/2} \frac{R_3(r)}{r^2}$	0.022	0.187
	0	$\frac{1}{2}c$	0	$-\sqrt{3}c^*/2$			
	0	$d/\sqrt{2}$	$-c/\sqrt{2}$	0			
	$-\frac{1}{2}a$	0	$-\sqrt{3}b/4$	0			
	0	0	0	$-b/\sqrt{2}$			
$\Phi_4^{M_J}$	$\frac{1}{4}b$	0	$\sqrt{3}a/2$	0	$\left(\frac{5}{4\pi}\right)^{1/2} \frac{R_4(r)}{r^2}$	0.080	0.292
	0	$\sqrt{3}a/2$	0	$\frac{1}{4}b$			
	$-b/\sqrt{2}$	0	0	0			
	0	$-\sqrt{3}b/4$	0	$-\frac{1}{2}a$			
	0	$-c^*/\sqrt{2}$	$d/\sqrt{2}$	0			
$\Phi_5^{M_J}$	$-c/2\sqrt{3}$	0	$-\frac{1}{2}c^*$	$2d/\sqrt{3}$	$\left(\frac{5}{4\pi}\right)^{1/2} \frac{R_5(r)}{r^2}$	0.004	0.002
	$d/\sqrt{6}$	$-c/\sqrt{2}$	0	$\sqrt{2/3}c^*$			
	$-\sqrt{2/3}c$	0	$c^*/\sqrt{2}$	$-d/\sqrt{6}$			
	$-2d/\sqrt{3}$	$\frac{1}{2}c$	0	$c^*/2\sqrt{3}$			
	0	$-d/\sqrt{2}$	$c/\sqrt{2}$	0			
$\Phi_6^{M_J}$	0	$\frac{1}{2}c^*$	d	$-\sqrt{3}c/2$	$\left(\frac{5}{4\pi}\right)^{1/2} \frac{R_5(r)}{r^2}$	0.004	0.002
	$-c/\sqrt{6}$	0	$-c^*/\sqrt{2}$	$-\sqrt{2/3}d$			
	$d/\sqrt{3}$	$\frac{1}{2}c$	0	$c^*/2\sqrt{3}$			
	$-c/2\sqrt{3}$	0	$-\frac{1}{2}c^*$	$-d/\sqrt{3}$			
	$\sqrt{2/3}d$	$c/\sqrt{2}$	0	$c^*/\sqrt{6}$			
	$\sqrt{3}c^*/2$	$-d$	$-\frac{1}{2}c$	0			

an extension of the commonly used *s*-like approximation. The scattering rates have been calculated for resonance absorption and for several second-order processes. Independently, Rayleigh scattering of phonons by isotopic impurities has also been evaluated. The black-body-radiation model is used to describe the phonon frequency distribution from the heat-pulse generator. A comparison of the heat-pulse data obtained with theoretical predictions based on the scattering mechanisms discussed above yielded reasonable agreement, both qualitatively and quantitatively, for a variety of conditions. The comparison was carried out by computer fitting of the theoretical results to the experimental data with the use of the valence-band-edge deformation-potential constants (characteristic for bound holes) as adjustable parameters, where-

by these constants were determined. The deformation-potential constants were considered separately in the contexts of static stress (such as the internal and the externally applied stresses) and dynamic stress (due to the thermal phonons). Typical differences of 30% were found between the corresponding static and dynamic constants. It is concluded that since the theory does not provide such a distinction, these differences reflect shortcomings in the basic description of the bound acceptor holes. These shortcomings include both the use of the effective-mass approximation, which is questionable in the case of Si, and the approximations used in its application, a source of errors particularly for Ge.

Some problems in using the heat-pulse technique and their possible influence on the results have

TABLE VII. The functions $\Phi_i^{M_J}$ for axis of quantization along [111]. $A = x^2 - y^2 - (2i/\sqrt{3})[z^2 - \frac{1}{2}(x^2 + y^2)]$, $B = xy + yz + zx$, $C = i[xy - \frac{1}{2}z(x+y)] + \frac{3}{2}z(x-y)$.

M_J	$\frac{3}{2}$	$\frac{1}{2}$
$\Phi_1^{M_J}$	0	$A^*/2\sqrt{2}$
	$\sqrt{3}A/4$	0
	$i\sqrt{3}A^*/4$	$-A/2\sqrt{2}$
	0	0
	0	$\frac{1}{4}A^*$
$\Phi_2^{M_J}$	0	$\frac{1}{4}iA^*$
	$IB/\sqrt{6}$	$\frac{1}{3}C^*$
	$C/\sqrt{6}$	$-\frac{2}{3}B$
	$-i\sqrt{2}C^*/\sqrt{3}$	$-\frac{1}{3}C$
	0	$B/3\sqrt{2}$
$\Phi_3^{M_J}$	0	$C/3\sqrt{2}$
	0	$-\frac{1}{3}i\sqrt{2}C^*$
	0	$-A^*/2\sqrt{2}$
	$-A/4\sqrt{3}$	0
	$iA^*/4\sqrt{3}$	$-A/2\sqrt{2}$
$\Phi_4^{M_J}$	$-A/\sqrt{6}$	0
	$-iA^*/\sqrt{6}$	$\frac{1}{4}A$
	0	$-\frac{1}{4}iA^*$
	$-B/\sqrt{6}$	$-\frac{1}{3}C^*$
	$-C/3\sqrt{6}$	0
$\Phi_5^{M_J}$	$-i\sqrt{2}C^*/3\sqrt{3}$	$-\frac{1}{3}C$
	$-2C/3\sqrt{3}$	$B/\sqrt{2}$
	$4iC^*/3\sqrt{3}$	$C/3\sqrt{2}$
	0	$\frac{1}{3}i\sqrt{2}C^*$
	0	$-\frac{1}{3}\sqrt{2}C^*$
$\Phi_6^{M_J}$	$2C/3\sqrt{3}$	0
	$iC^*/3\sqrt{3}$	$-\frac{1}{3}\sqrt{2}C$
	$\sqrt{2}C/3\sqrt{3}$	0
	$i\sqrt{2}C^*/3\sqrt{3}$	$-\frac{2}{3}C$
	$i\sqrt{2}B/\sqrt{3}$	$-\frac{1}{3}iC^*$

been discussed. These include the limitations of the black-body-radiation model, and the presence of scattered phonons in the detected pulses. Furthermore, at sufficiently high impurity contents, a local increase in the density of phonons in the vicinity of the generator is believed to occur and to produce an additional broadening of the resonance. This broadening is thought to increase the over-all scattering of phonons in the heat pulses at low to intermediate stresses, consistent with the experimental observations on the highly doped Si samples. A consistent overestimation by the theory of the

received pulse amplitude at small external stresses is accounted for in terms of internal stresses. Values for average internal stresses (at the impurity sites) have been deduced by comparing theory and experiment, and are found to be typically $1-3 \times 10^8$ dyn/cm² for the samples investigated.

APPENDIX A

Table VI shows the wave-function components $\Phi_i^{M_J}$ [Eq. (2.1)] in the (M_2, M_5) bases with axis of quantization along the [001] direction. These have been computed in the ($s+d$)-like approximation according to the prescription by SOH.¹³ Each vector in Table VI is normalized to unity when the radial part is normalized, i. e.,

$$\int_0^\infty R_i^2(r)r^2 dr = 1, \quad i = 0, \dots, 5. \quad (\text{A1})$$

The radial forms are chosen to be of the simplest possible form with¹³

$$R_0(r) = (4/r_1^3)^{1/2} e^{-r/r_1}, \quad (\text{A2})$$

$$R_i(r) = (8/45r_2^7)^{1/2} r^2 e^{-r/r_2}, \quad i = 1, \dots, 5.$$

For Si and Ge SOH give the effective Bohr radii $r_1 = 15.0$ Å, $r_2 = 11.1$ Å and $r_1 = 37.8$ Å, $r_2 = 29.9$ Å, respectively. Table VI also lists the amplitude factors C_i ($i = 0, \dots, 5$) obtained by SOH.

In Table VII the functions $\Phi_i^{M_J}$ ($M_J = \frac{3}{2}, \frac{1}{2}$) are presented for axis of quantization along [111]. These were obtained by decomposing the generating operators (see SOH) along the axes of a new coordinate system with z' axis along [111].

APPENDIX B

The coupling parameters $C_{qt}^{nm'}$ are related in the following way:

$$C_{qt}^{11} = C_{qt}^{44} = -C_{qt}^{22} = -C_{qt}^{33},$$

$$C_{qt}^{12} = -C_{qt}^{34}, \quad C_{qt}^{13} = C_{qt}^{24}, \quad (\text{B1})$$

$$C_{qt}^{14} = C_{qt}^{23} = 0, \quad C_{qt}^{nm'} = (C^{n'n})^*.$$

For the axis of quantization along [001] $C_{qt}^{nm'}$ is given by

$$C_{qt}^{11} = \frac{1}{2} D (2\hat{q}_z e_{tq}^z - \hat{q}_x e_{tq}^x - \hat{q}_y e_{tq}^y),$$

$$C_{qt}^{12} = \frac{1}{2} \sqrt{3} [(\hat{q}_z e_{tq}^x + \hat{q}_x e_{tq}^z) - i(\hat{q}_z e_{tq}^y + \hat{q}_y e_{tq}^z)], \quad (\text{B2})$$

$$C_{qt}^{13} = \frac{1}{2} \sqrt{3} [D(\hat{q}_x e_{tq}^x - \hat{q}_y e_{tq}^y) - (\hat{q}_x e_{tq}^y \hat{q}_y e_{tq}^x)],$$

and for [111]

TABLE VIII. Coupling parameters $C_{qt}^{nm'}$ for axis of quantization along [001] in the quasi-isotropic approximation.

t	1	2	3
C_{qt}^{11}	$\frac{1}{2} D (3\cos^2\theta - 1)$	$-\frac{3}{4} D \sin 2\theta$	0
C_{qt}^{12}	$\frac{1}{2} \sqrt{3} \sin 2\theta (\cos\phi - i \sin\phi)$	$\frac{1}{2} \sqrt{3} \cos 2\theta (\cos\phi - i \sin\phi)$	$-\frac{1}{2} \sqrt{3} \cos\theta (\sin\phi - i \cos\phi)$
C_{qt}^{13}	$\frac{1}{2} \sqrt{3} D \sin^2\theta \cos 2\phi - \frac{1}{2} \sqrt{3} \sin^2\theta \sin 2\phi$	$\frac{1}{4} \sqrt{3} D \sin 2\theta \cos 2\phi - \frac{1}{4} \sqrt{3} \sin 2\theta \sin 2\phi$	$-\frac{1}{2} \sqrt{3} D \sin\theta \sin 2\phi + \frac{1}{2} \sqrt{3} \sin\theta \cos 2\phi$

TABLE IX. X_{1t} , X_{2t} , Y_{1t} , Y_{2t} , and C_{qt}^{11} in the quasi-isotropic approximation, for stress along [111].

t	1	2	3
C_{qt}^{11}	$\frac{1}{2} \sin^2\theta \sin 2\phi$ $+\frac{1}{2} \sin 2\theta(\sin\phi + \cos\phi)$	$-\frac{1}{4} \sin 2\theta \sin 2\phi - \frac{1}{2} \cos 2\theta$ $\times (\cos\phi + \sin\phi)$	$-\frac{1}{2} \sin\theta \cos 2\phi$ $-\frac{1}{2} \cos\theta(\cos\phi$ $-\sin\phi)$
X_{1t}	$(D/\sqrt{2}) \sin^2\theta \cos 2\phi$	$-(D/2\sqrt{2}) \sin 2\theta \cos 2\phi$	$(D/\sqrt{2}) \sin\theta \sin 2\phi$
X_{2t}	$(1/2\sqrt{2}) \sin 2\theta (\cos\phi - \sin\phi)$	$-(1/2\sqrt{2}) \cos 2\theta (\cos\phi - \sin\phi)$	$(1/2\sqrt{2}) \cos\theta (\cos\phi$ $+\sin\phi)$
Y_{1t}	$(D/\sqrt{6}) (3\cos^2\theta - 1)$	$\frac{1}{2} D \sqrt{\frac{3}{2}} \sin 2\theta$	0
Y_{2t}	$-(1/\sqrt{6}) [2\sin^2\theta \cos 2\phi - \sin 2\theta$ $\times (\sin\phi + \cos\phi)]$	$(1/2\sqrt{6}) [\sin 2\theta \cos 2\phi$ $-\cos 2\theta (\sin\phi + \cos\phi)]$	$(1/2\sqrt{6}) [2\sin\theta \cos 2\phi$ $-\cos\theta (\cos\phi$ $-\sin\phi)]$

$$C_{qt}^{11} = \frac{1}{2} [\hat{q}_x (e_{iq}^y + e_{iq}^z) + \hat{q}_y (e_{iq}^x + e_{iq}^z) + \hat{q}_z (e_{iq}^x + e_{iq}^y)],$$

$$C_{qt}^{12} = (D/\sqrt{2}) (\hat{q}_x e_{iq}^x - \hat{q}_y e_{iq}^y) + (1/2\sqrt{2}) (\hat{q}_x e_{iq}^x + \hat{q}_z e_{iq}^z - \hat{q}_x e_{iq}^y - \hat{q}_y e_{iq}^z) - i \{ (D/\sqrt{6}) (\hat{q}_x e_{iq}^x + \hat{q}_y e_{iq}^y - 2\hat{q}_z e_{iq}^z) \\ - (1/2\sqrt{6}) [2(\hat{q}_y e_{iq}^x + \hat{q}_x e_{iq}^y) - (\hat{q}_z e_{iq}^y + \hat{q}_y e_{iq}^z) - (\hat{q}_z e_{iq}^x + \hat{q}_x e_{iq}^z)] \},$$

$$C_{qt}^{13} = (D/2\sqrt{3}) (\hat{q}_x e_{iq}^x + \hat{q}_y e_{iq}^y - 2\hat{q}_z e_{iq}^z) - (1/2\sqrt{3}) [2(\hat{q}_y e_{iq}^x + \hat{q}_x e_{iq}^y) \\ - (\hat{q}_z e_{iq}^y + \hat{q}_y e_{iq}^z) - (\hat{q}_z e_{iq}^x + \hat{q}_x e_{iq}^z)] \\ + i [-\frac{1}{2} D (\hat{q}_x e_{iq}^x - \hat{q}_y e_{iq}^y) + \frac{1}{2} (\hat{q}_z e_{iq}^x - \hat{q}_z e_{iq}^y - \hat{q}_y e_{iq}^z + \hat{q}_x e_{iq}^z)].$$

(B3)

x , y and z here always refer to the fourfold axes [001], [010], and [001], respectively. \hat{q}_α is the direction cosine of the wave vector with respect to the α axis. e_{iq}^α is the α component of the polarization vector corresponding to a phonon of wave vectors q in branch t . $D = D_w/D_{it}$. The coupling parameters C_{qt}^{nr} have also been rewritten in terms of the quasi-isotropic approximation (Table I). These are shown in Table VIII for the three acous-

tical branches, for axis of quantization along [001]. With the axis of quantization along [111], C_{qt}^{nr} can be written

$$C_{qt}^{12} = X_{1t} + X_{2t} + i(Y_{1t} + Y_{2t}), \\ C_{qt}^{13} = -(1/\sqrt{2})Y_{1t} + \sqrt{2}Y_{2t} + i[-(1/\sqrt{2})X_{2t}],$$

(B4)

where X_{1t} , X_{2t} , Y_{1t} , and Y_{2t} , along with C_{qt}^{11} are given in Table IX.

*Research supported in part by the National Science Foundation and by the Advanced Research Projects Agency.

¹Present address: Max-Planck-Institut für Festkörperforschung, Heilbronner Strasse 69, 7000 Stuttgart 1, Germany.

²NASA International University Fellow. Present address: Electrotechnical Laboratory, 5-4-1 Mukodai, Tanashi, Tokyo, Japan.

³R. W. Keyes, Phys. Rev. **122**, 1176 (1961).

⁴A. Griffin and P. Carruthers, Phys. Rev. **131**, 1976 (1963).

⁵J. F. Goff and N. Pearlman, Phys. Rev. **140**, A2151 (1965).

⁶M. P. Mathur and N. Pearlman, Phys. Rev. **180**, 833 (1969).

⁷J. A. Carruthers, T. H. Geballe, H. M. Rosenberg, and J. M. Ziman, Proc. R. Soc. A **238**, 502 (1957).

⁸J. A. Carruthers, J. F. Cochran, and K. Mendelsohn, Cryogenics **2**, 160 (1962).

⁹M. G. Holland and L. S. Neuringer, in *Proceedings of the International Conference on Semiconductor Physics, Exeter, 1962* (The Physical Society, London, 1962), p. 474.

¹⁰M. Pomerantz and R. J. von Gutfeld, in *Proceedings of the International Conference on Semiconductor Physics, Moscow, 1968* (NAUKA, Leningrad, 1968), Vol. 2, p. 690.

¹¹W. Kohn, in *Solid State Physics*, edited by F. Seitz and D. Turnbull (Academic, New York, 1957), Vol. 5, p. 257.

¹²K. Suzuki and N. Mikoshiba, Phys. Rev. B **3**, 2550 (1971).

¹³K. Suzuki and N. Mikoshiba, J. Phys. Soc. Jap. **31**, 44 (1971).

¹⁴T. Ishiguro, T. A. Fjeldly, and C. Elbaum, Phys. Rev. Lett. **27**, 667 (1971).

¹⁵K. Suzuki, M. Okazaki, and H. Hasegawa, J. Phys. Soc. Jap. **19**, 930 (1964).

¹⁶H. Hasegawa, Phys. Rev. **102**, 1029 (1963).

¹⁷J. C. Hensel and G. Feher, Phys. Rev. **129**, 1041 (1963).

¹⁸K. Suzuki and N. Mikoshiba, Phys. Rev. B **4**, 2822 (1971).

¹⁹T. A. Fjeldly, Ph.D. thesis (Brown University, 1972) (unpublished).

²⁰H. Hasegawa, Phys. Rev. **118**, 1523 (1960).

²¹F. I. Fedorov, *Theory of Elastic Waves in Crystals* (Plenum, New York, 1968).

²²P. Kwok, Phys. Rev. **149**, 666 (1966).

²³P. G. Klemens, Proc. Phys. Soc. Lond. A **68**, 1113 (1955).

²⁴M. G. Holland, Phys. Rev. **132**, 2461 (1963).

²⁵V. Narayanamurti, Phys. Lett. A **30**, 521 (1969).

²⁶W. A. Little, Can. J. Phys. **37**, 334 (1959).

²⁵H. Stanton, Ph.D. thesis (Brown University, 1969) (unpublished).

²⁶I. Gerstein and C. Elbaum (unpublished).

²⁷R. J. von Gutfeld, in *Physical Acoustics*, edited by W. P. Mason (Academic, New York, 1968), Vol. 5, p. 233.

²⁸B. Taylor, H. J. Maris, and C. Elbaum, *Phys. Rev. B* **3**, 1462 (1971).

²⁹B. Taylor, Ph.D. thesis (Brown University, 1970) (unpublished).

³⁰H. J. Maris, *J. Acoust. Soc. Am.* **50**, 812 (1970).

³¹J. J. Hall, *Phys. Rev.* **128**, 68 (1962).

³²A. M. Glass, *Can. J. Phys.* **43**, 12 (1965).

³³I. Balsev, *Solid State Commun.* **5**, 315 (1967).

³⁴F. H. Pollak and M. Cardona, *Phys. Rev.* **172**, 816 (1968).

³⁵R. L. Jones and P. Fisher, *Phys. Rev. B* **2**, 2016 (1970).

³⁶L. D. Laude, F. H. Pollak, and M. Cardona, *Phys. Rev. B* **3**, 2623 (1970).

³⁷I. Balsev, *Phys. Rev.* **143**, 636 (1966).

³⁸I. P. Akimchenko and V. A. Vdovenkov, *Fiz. Tverd. Tela* **11**, 658 (1969) [*Sov. Phys.-Solid State* **11**, 528 (1969)].

³⁹R. Truell, C. Elbaum, and B. B. Chick, *Ultrasonic Methods in Solid State Physics* (Academic, New York, 1969).

PHYSICAL REVIEW B

VOLUME 7, NUMBER 4

15 FEBRUARY 1973

Calculation of the Thermal Expansion for a Quasiharmonic Model of Tellurium*

T. G. Gibbons

*Division of Chemistry, National Research Council of Canada,
Ottawa, Ontario, Canada K1A 0R6*

(Received 2 June 1972)

A simple quasiharmonic model, employing a valence-force approach, is used to calculate the Grüneisen functions and thermal expansion of tellurium. The calculations illustrate the use of a new thermodynamic formalism for treating internal strain and reveal explicitly the effect that an internal degree of freedom has upon the macroscopic properties. The valence-force picture of tellurium is critically discussed in the light of a comparison of the calculations with experiment. Suggestions are made for further experimental work and for improvements in the theoretical model.

I. INTRODUCTION

The present paper is concerned with the application of quasiharmonic theory to calculate the Grüneisen functions and thermal expansion for a simple lattice-dynamical model of tellurium. The structure of tellurium consists of parallel helical chains of atoms, disposed in an hexagonal array, and belongs to the space group D_3^4 or D_3^6 (see Fig. 1), in the Schoenflies notation, equivalent to $P3_121$ or $P3_221$ in the Hermann-Mauguin notation, where the alternatives represent helices of opposite handedness. The neighboring element in group VIb, selenium, also has this structure but the present calculations are applied specifically to tellurium since this has been far more widely studied experimentally.

A considerable amount of experimental data are available for comparison with "harmonic" lattice models. The zone-center optic frequencies have been measured by infrared^{1,2} and, more recently, Raman studies.^{3,4} Using coherent neutron scattering, Powell and Martel⁵ have measured phonon dispersion curves along certain high-symmetry directions and their measurements correlate well with the optical measurements, and also with frequency spectra obtained from earlier neutron work of Kotov *et al.*⁶ and Gissler and Axmann⁷ (although the former's value for the highest-frequency peak appears to be a little high). Data also exist for the

elastic constants⁸ between 100 and 300 °K and the specific heat⁹⁻¹¹ down to 1 °K.

The thermal-expansion coefficients of a_{\perp} and a_{\parallel} of tellurium have been measured by a variety of techniques¹²⁻¹⁷ at temperatures from 2 up to 500 °K, and the different measurements are in reasonably close agreement with each other. The data have been analyzed in terms of the Grüneisen functions γ_{\perp} and γ_{\parallel} , and, as for the thermal expansion, the behavior is strongly anisotropic. The tellurium structure retains an internal degree of freedom during thermal expansion so that an internal expansion coefficient can also be measured.¹⁵

Before applying quasiharmonic theory to calculate the thermal expansion it was necessary to begin with a harmonic model which was reasonably compatible with experiment but which allowed anharmonicity to be introduced in a straightforward and meaningful way. For this reason a model was chosen based on that of Hulin¹⁸ and using a force field approach similar to the models put forward by Geick and Schröder¹⁹ and Nakayama *et al.*²⁰ The shortcomings of these models are pointed out but they are preferable to the more successful model of Pine and Dresselhaus⁴ which involves too many adjustable parameters and is too generalized for present purposes.

As mentioned above, when tellurium expands on heating it maintains an internal degree of freedom.

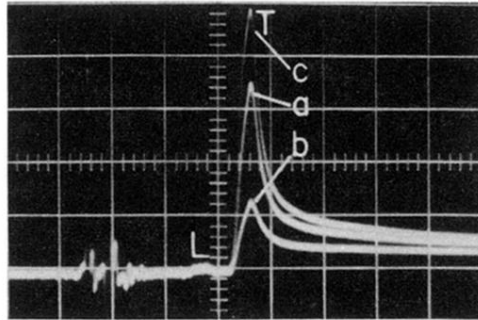


FIG. 1. Heat pulses in sample p -Si 15A. Input power, 0.3 W (i. e., $T_{\text{pulse}} = 6.5$ K as determined from the black-body theory). Vertical and horizontal scales are 0.05 V/div. and $0.2 \mu\text{sec/div.}$, respectively. The propagation is along the [100] direction, a distance of 3.2 mm. a , b , and c are pulses for external stresses 0, 5.3, and 11.4 ($\times 10^8 \text{ dyn/cm}^2$), respectively, along the [001] direction.

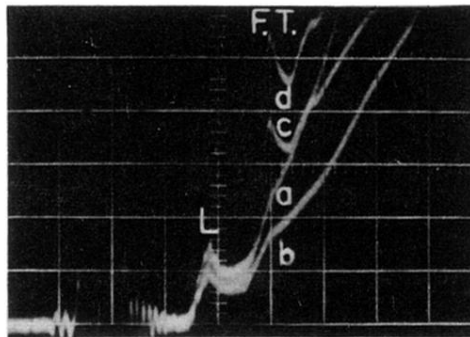


FIG. 2. Heat pulses in sample p -Si 16B. Input power, 3.9 W (i. e., $T_{\text{pulse}} = 12.1$ K as determined from the black-body theory). Vertical and horizontal scales are 0.02 V/div. and 0.2 $\mu\text{sec}/\text{div.}$, respectively. The propagation is along the $[\bar{1}\bar{1}0]$ direction, over a distance of 3.8 mm. a , b , c , and d are pulses for external stresses 0, 2.0, 4.2, and 4.7 ($\times 10^8$ dyn/cm 2), respectively, along the $[111]$ direction. F. T. denotes the fast-transverse pulse and L the longitudinal pulse.